

CHANDRA X-RAY AND HUBBLE SPACE TELESCOPE IMAGING OF OPTICALLY SELECTED KILOPARSEC-SCALE BINARY ACTIVE GALACTIC NUCLEI. I. NATURE OF THE NUCLEAR IONIZING SOURCES*

XIN LIU^{1,3}, FRANCESCA CIVANO¹, YUE SHEN¹, PAUL GREEN¹, JENNY E. GREENE², AND MICHAEL A. STRAUSS²

¹Harvard-Smithsonian Center for Astrophysics, 60 Garden Street, Cambridge, MA 02138, USA

²Department of Astrophysical Sciences, Princeton University, Peyton Hall, Ivy Lane, Princeton, NJ 08544, USA

Received 2012 September 22; accepted 2012 November 20; published 2012 December 20

ABSTRACT

Kiloparsec-scale binary active galactic nuclei (AGNs) signal active supermassive black hole (SMBH) pairs in merging galaxies. Despite their significance, unambiguously confirmed cases remain scarce and most have been discovered serendipitously. In a previous systematic search, we optically identified four kpc-scale binary AGNs from candidates selected with double-peaked narrow emission lines at $z = 0.1\text{--}0.2$. Here, we present *Chandra* and *Hubble Space Telescope* Wide Field Camera 3 (WFC3) imaging of these four systems. We critically examine and confirm the binary-AGN scenario for two of the four targets, by combining high angular resolution X-ray imaging spectroscopy with *Chandra* ACIS-S, better nuclear position constraints from WFC3 F105W imaging, and direct starburst estimates from WFC3 F336W imaging; for the other two targets, the existing data are still consistent with the binary-AGN scenario, but we cannot rule out the possibility of only one AGN ionizing gas in both merging galaxies. We find tentative evidence for a systematically smaller X-ray-to-[O III] luminosity ratio and/or higher Compton-thick fraction in optically selected kpc-scale binary AGNs than in single AGNs, possibly caused by a higher nuclear gas column due to mergers and/or a viewing angle bias related to the double-peak narrow-line selection. While our result lends some further support to the general approach of optically identifying kpc-scale binary AGNs, it also highlights the challenge and ambiguity of X-ray confirmation.

Key words: black hole physics – galaxies: active – galaxies: interactions – galaxies: nuclei – galaxies: Seyfert – quasars: general – X-rays: galaxies

Online-only material: color figures

1. INTRODUCTION

1.1. Significance of Binary Supermassive Black Holes

Most bulge-dominated galaxies harbor central supermassive black holes (SMBHs; Kormendy & Richstone 1995). As a result, binary⁴ SMBHs are expected to form in galaxy mergers (Begelman et al. 1980; Milosavljević & Merritt 2001; Yu 2002); they are an inevitable and important consequence of the hierarchical bulge and SMBH formation process. Binary SMBHs are believed to have a significant dynamical impact on the nuclear stellar structure of massive elliptical galaxies (e.g., Faber et al. 1997; Ravindranath et al. 2002; Graham 2004; Merritt 2006; Kormendy & Bender 2009). The final inspiral and coalescence of hardened SMBH binaries are predicted to produce strong gravitational wave signals (Thorne & Braginskii 1976), the detection of which would offer a direct test of general relativity on cosmological scales (Thorne 1987). The identification and characterization of binary SMBHs at various merger phases are valuable both for understanding galaxy/SMBH

evolution and for probing fundamental physics (see a comprehensive review by Colpi & Dotti 2011).

1.2. Binary AGNs: the Kiloparsec Scales

The frequency and statistical properties of binary active galactic nuclei (AGNs) may offer useful insights into the hierarchical merger paradigm of galaxy evolution (Yu et al. 2011) and the role of mergers in AGN fueling⁵ (Ellison et al. 2011; Liu et al. 2012b; Silverman et al. 2011; Van Wassenhove et al. 2012). In a galaxy merger, if both black holes (BHs) are simultaneously accreting, then they can be detected through spatially resolved emission diagnostics which signal the presence of two AGNs. Theory suggests that merger-induced gas inflows become significant (therefore likely triggering AGNs) at separations under about a kpc (Hernquist 1989). Unlike the bound binary phase, which is still extremely challenging to image directly (e.g., Burke-Spolaor 2011), the “pairing” phase (where the separation between the two BHs, a , is a few tens pc to a few tens kpc) is the most accessible because the two BHs are still resolvable at cosmological distances (typical

* Based, in part, on observations made with the NASA/ESA *Hubble Space Telescope*, obtained at the Space Telescope Science Institute, which is operated by the Association of Universities for Research in Astronomy, Inc., under NASA contract NAS 5-26555. These observations are associated with program number GO 12363.

³ Einstein Fellow.

⁴ Following the initial nomenclature of Komossa et al. (2003) for NGC 6240, we use “binary” AGNs to denote a pair of AGNs, also in line with the nomenclature “binary quasars” adopted in the literature. In this context, “binary” does not necessarily presume that the black holes themselves are gravitationally bound to each other (e.g., in the case of kpc-scale binary AGNs, the host galaxies dominate the potential well).

⁵ While the small-scale ($\sim 0.1\text{--}1$ Mpc) quasar–quasar two-point correlation function suggests a clustering excess over the large-scale (> 1 Mpc) extrapolation (Hennawi et al. 2006; Myers et al. 2007; Hennawi et al. 2010; Shen et al. 2010), it is still unclear whether this is due to tidally enhanced BH accretion (e.g., Djorgovski 1991; Kochanek et al. 1999; Mortlock et al. 1999), or is rather due to the small-scale clustering of their host dark matter halos (e.g., Hopkins et al. 2008; Green et al. 2011; Richardson et al. 2012). The projected separations of most of the observed binary quasars are on scales of tens of kpc and larger, which may still be too large for galaxy–galaxy tidal interactions to be effective (but see Green et al. 2010 for a counterexample of a 21 kpc separation binary quasar observed to have tidal features indicative of ongoing interaction).

separation $\gtrsim 1''$). Of particular interest is the late-pairing phase ($a < 10$ kpc), which connects mergers in a cosmological context to pairs of BHs in galaxies, and sets the stage for the subsequent evolution of close binaries.

1.3. Systematic Searches for kpc-scale Binary AGNs

The past few years have seen a significant increase in the inventory of kpc-scale binary AGNs, both from serendipitous discoveries and from systematic searches. While the existence of kpc-scale binary AGNs has been confirmed in a few pioneering early discoveries (Moran et al. 1992; Komossa et al. 2003; Hudson et al. 2006; Bianchi et al. 2008) and further verified by more recent studies in X-rays (Brassington et al. 2007; Fabbiano et al. 2011; Koss et al. 2011; Mazzarella et al. 2012; see also Comerford et al. 2011 for a candidate), radio (Fu et al. 2011b; Tadhunter et al. 2012), and optical broad emission lines (Junkkarinen et al. 2001; Shields et al. 2012), the frequency of occurrence and statistical properties of these systems remain poorly constrained.

Addressing the frequency and statistical properties of binary AGNs requires systematic searches. A natural approach is to select candidates in galaxy mergers with double nuclei and follow up to identify binary AGNs using diagnostic observations such as X-ray imaging (Guainazzi et al. 2005; Piconcelli et al. 2010; Koss et al. 2012; Teng et al. 2012) and/or spatially resolved optical spectroscopy (Barth et al. 2008; Comerford et al. 2009b⁶; Green et al. 2010; Greene et al. 2011; Liu et al. 2011; Shields et al. 2012). However, because of the requirement that the two nuclei be resolved in ground-based optical imaging, systems identified using this approach are generally biased against the late-pairing phase.

To mitigate this bias, an alternative approach is to select candidates by kinematic signatures in spatially integrated spectra, in analogy to the case of spectroscopic binary stars. In particular, one such signature is the few hundred km s^{-1} velocity splitting observed in AGN narrow emission lines (NELs; e.g., Sargent 1972; Heckman et al. 1981) such as [O III] $\lambda\lambda 4959, 5007$, which is seen in $\sim 1\%$ of low-redshift AGNs (Liu et al. 2010b; Smith et al. 2010; Wang et al. 2009; Ge et al. 2012) as well as in quasars (Shen et al. 2011b). The working hypothesis is that the velocity splitting signals the projected relative orbital motion of two narrow-line regions (NLRs), each ionized by its own central AGN (e.g., Zhou et al. 2004; Gerke et al. 2007; Comerford et al. 2009a; Xu & Komossa 2009; Peng et al. 2011; Barrows et al. 2012). By selection, only binaries with projected angular separations smaller than the spectroscopic aperture size will be included. In principle, binary AGNs with separations as small as a few tens of pc (limited by the intrinsic size of NLRs, which are ~ 50 – 1000 pc, and scale approximately as $L^{0.5}$; Schmitt et al. 2003; Bennert et al. 2002) may be identified, if the associated double stellar nuclei are resolvable by follow-up observations using higher resolution near-infrared (NIR) imaging with *HST* and/or ground-based adaptive optics (AO). Therefore, this kinematics approach should be well suited for identifying binary SMBHs in the late-pairing phase.

A major obstacle in identifying binary AGNs using the NEL splitting signature, however, is that such profiles can also arise from NLR gas kinematics around single AGNs, such as rotating disks or bi-conical outflows (Axon et al. 1998; Veilleux et al. 2001; Crenshaw et al. 2010; Shen et al. 2011a; Rosario

et al. 2010; Fischer et al. 2011; Smith et al. 2011, 2012). Nevertheless, our follow-up observations (Liu et al. 2010a; Shen et al. 2011a) of a subset of a systematically selected sample of 167 AGNs with double-peaked NELs (Liu et al. 2010b; see also Smith et al. 2010; Wang et al. 2009), as well as studies by other groups (McGurk et al. 2011; Fu et al. 2012), have demonstrated the feasibility and importance of combining higher resolution NIR imaging (Fu et al. 2011a; Rosario et al. 2011) and spatially resolved optical spectroscopy (Comerford et al. 2012) to discriminate kpc-scale binary AGNs from single-AGN-NLR gas kinematics. Kpc-scale binary AGNs tend to show two concentrated [O III] nuclei spatially coincident with two stellar bulges in a merger, with the dynamics dominated by the potential of the individual stellar bulges. Objects with complex NLR kinematics, in contrast, usually exhibit bi-cone/disk-shaped diffuse [O III] with a smooth single-peaked stellar background, also illustrated by the local example Mrk 78 (Whittle & Wilson 2004; Fischer et al. 2011). Roughly 10% of the objects we have followed up are best explained by binary AGNs at (projected) kpc-scale separations.

1.4. This Work: High-resolution Optical and X-Ray Imaging of Optically Identified kpc-scale Binary AGNs

Here and in a companion paper (Liu et al. 2012a, hereafter Paper II), we present F336W/*U*- and F105W/*Y*-band images obtained using Wide Field Camera 3 (WFC3) on board the *Hubble Space Telescope* (*HST*), and 0.5–10 keV X-ray images taken with the *Chandra X-ray Observatory* (Weisskopf et al. 1996) Advanced CCD Imaging Spectrometer (ACIS; Garmire et al. 2003) of the four optically selected kpc-scale binary AGNs identified by Liu et al. (2010a). Although our ground-based NIR imaging and spatially resolved optical spectroscopy strongly suggest that these galaxy mergers host binary AGNs (Liu et al. 2010a; Shen et al. 2011a), the case is not watertight. While seven of the eight NEL nuclei in the four galaxies are optically classified as Type 2 Seyferts, one [O III]-faint nucleus is optically classified as either a Type 2 Seyfert, a LINER, or a LINER–H II composite, the latter two cases of which may be due to starburst and/or shock heating rather than AGN excitation (e.g., Lutz et al. 1999; Terashima et al. 2000; Eracleous et al. 2002). More importantly, even in the ‘‘Seyfert–Seyfert’’ cases, there could be only one AGN, which ionizes gas in both merging components (e.g., Moran et al. 1992). Photoionization arguments based on spatially resolved optical spectroscopy were unable to rule out this possibility (Liu et al. 2010a), given that the nuclear separation is not much larger than the sizes of individual NLRs, and the large systematic uncertainties in the electron density measurements from diagnostic emission-line ratios.

The motivation of our present work is to further clarify these ambiguities concerning the nature of the ionizing sources in optically selected kpc-scale binary AGNs. *HST*/WFC3’s *Y*-band images allow us to get better positional priors to resolve the closely separated double nuclei in X-ray imaging; the *U*-band images offer constraints on spatially resolved star formation activity in the host galaxy (Section 3.1). Utilizing *Chandra* ACIS’s superb spatial resolution and imaging spectroscopy capability in X-rays (Section 3.2), we put more direct constraints on the intrinsic X-ray luminosity for each individual nucleus in the merging galaxies than on those estimates inferred empirically from [O III] $\lambda 5007$ emission-line luminosity (Section 4.1). Combined with constraints on the contribution from star formation to the observed X-ray luminosities estimated from *U*-band imaging (Section 4.2), we critically examine the purported binary-AGN

⁶ But see Civano et al. (2010, 2012) and Blecha et al. (2012a) for an alternative explanation for this particular candidate.

Table 1
Kpc-scale Binary-AGN Candidates Imaged with *HST*/WFC3 and *Chandra* X-Ray Observatory/ACIS

Target Name	Plate	Fiber	MJD	Redshift	<i>HST</i>	$\Delta\theta_Y$	$r_{p,Y}$	<i>Chandra</i>	$\Delta\theta_{X\text{-ray}}$
(1)	(2)	(3)	(4)	z_c	Obs. UT	($''$)	(kpc)	Obs. UT	($''$)
				(5)	(6)	(7)	(8)	(9)	(10)
SDSS J110851.04+065901.4	1004	182	52723	0.1816	20110513	0.70	2.1	20110210	0.82
SDSS J113126.08−020459.2	327	394	52294	0.1463	20110524	0.70	1.8	20110211	...
SDSS J114642.47+511029.6	881	241	52368	0.1300	20110620	2.71	6.3	20110423	3.03
SDSS J133226.34+060627.4	1801	250	54156	0.2070	20110310	1.50	5.1	20111128	...

Notes. Column 1: SDSS names with J2000 coordinates given in the form of “hhmmss.ss+ddmmss.s.” Columns 2–4: SDSS spectroscopic plate number, fiber ID, and Modified Julian Date. Column 5: systemic redshift measured from stellar continuum absorption features in the SDSS fiber spectra. Columns 6 and 9: dates of the *HST* and *Chandra* observations. Columns 7 and 8: projected angular and physical separation between the double nuclei measured from *HST* *Y*-band images. Column 10: angular separation between the double nuclei measured from ACIS X-ray images. See Table 2 for measured positions of the individual nuclei.

Table 2
HST/WFC3 *Y*-band and *Chandra*/ACIS X-Ray 0.2–10 keV Astrometry of the Double Nuclei

Object Name	Redshift	$\log L_{[\text{O III}]}$ ^{obs}	$\log L_{[\text{O III}]}$ ^{cor}	R.A. _{<i>Y</i>}	Decl. _{<i>Y</i>}	R.A. _{X-ray}	Decl. _{X-ray}	$\Delta\theta_{\text{diff}}$
(1)	z_c	(erg s^{-1})	(erg s^{-1})	(J2000)	(J2000)	(J2000)	(J2000)	($''$)
	(2)	(3)	(4)	(5)	(6)	(7)	(8)	(9)
SDSS J1108+0659NW	0.1812	42.16	42.66	11:08:51.029	+06:59:01.32	11:08:51.031	+06:59:01.26	0.07
SDSS J1108+0659SE	0.1820	41.52	41.64	11:08:51.061	+06:59:00.81	11:08:51.069	+06:59:00.66	0.19
SDSS J1131−0204W	0.1454	41.40	42.34	11:31:26.042	−02:04:59.33
SDSS J1131−0204E	0.1470	41.31	42.22	11:31:26.088	−02:04:59.21
SDSS J1146+5110SW	0.1293	41.93	42.18	11:46:42.466	+51:10:29.46	11:46:42.504	+51:10:29.45	0.36
SDSS J1146+5110NE	0.1303	41.38	41.65	11:46:42.630	+51:10:31.69	11:46:42.672	+51:10:32.03	0.52
SDSS J1332+0606SW	0.2057	41.06	41.64	13:32:26.340	+06:06:27.31
SDSS J1332+0606NE	0.2074	41.83	42.84	13:32:26.372	+06:06:28.73	13:32:26.364	+06:06:28.63	0.16

Notes. Column 2: emission-line redshift measured from spatially resolved optical spectra (Liu et al. 2010a). Column 3: observed [O III] λ 5007 emission-line luminosity measured from spatially resolved optical spectra (Liu et al. 2010a). Columns 4 and 5: coordinates of the double nuclei measured from *HST* *Y*-band images. Typical absolute (relative) astrometric uncertainty is $0''.2$ ($0''.01$); Columns 6 and 7: coordinates measured from ACIS images. Typical absolute (relative) astrometric uncertainty is $0''.2$ ($0''.15$). See Section 3.2.1 for details; Columns 8 and 9: difference between the X-ray and *Y*-band measured positions.

nature of our targets (Section 4.3). Combining the new X-ray observations with our previous optical spectroscopy, we tentatively characterize the fraction of optical binary AGNs that are weak or Compton-thick X-ray emitters, and compare with the fraction among single AGNs (Section 4.4). Since our targets were selected in a systematic search, our results have general implications for the general approach of identifying kpc-scale binaries in double-peaked AGNs (Section 5.1), the attributes and limitations of optical identification compared to X-ray searches (Section 5.2), and the frequency of kpc-scale binary AGNs (Section 5.3).

Throughout this paper, we assume a concordance cosmology with $\Omega_m = 0.3$, $\Omega_\Lambda = 0.7$, and $H_0 = 70 \text{ km s}^{-1} \text{ Mpc}^{-1}$, and use the AB magnitude system (Oke 1974).

2. TARGET SELECTION AND PROPERTIES

In Table 1, we list basic photometric and spectroscopic properties of the four binary-AGN candidates. These candidates were discovered from a subset of a parent sample of 167 Type 2 AGNs with double-peaked [O III] $\lambda\lambda$ 4959,5007 emission lines (Liu et al. 2010b). The parent sample was identified from 14,756 Type 2 AGNs optically selected from the spectroscopic catalog of the Sloan Digital Sky Survey (SDSS; York et al. 2000) Data Release Seven (DR7; Abazajian et al. 2009). We focused on Type 2 (i.e., obscured) AGNs, which allow us to study the host galaxy properties without much contamination from the AGNs. The optical emission-line ratios [O III] λ 5007/H β and [N II] λ 6584/H α are characteristic of Type 2 Seyferts according to the Kewley et al. (2001) criterion based on the Baldwin et al.

(1981) diagnostics. We obtained ground-based deep NIR images and optical slit spectra from the Magellan 6.5 m and the Apache Point Observatory 3.5 m telescopes (Liu et al. 2010a; Shen et al. 2011a). We identified four strong kpc-scale binary-AGN candidates out of 43 objects observed⁷ (Liu et al. 2010a). In each system, the NIR images reveal tidal features and double stellar components with a projected separation of several kpc, while optical slit spectra show two Type 2 Seyfert nuclei (except for one nucleus, which could also be a LINER or a composite) spatially coincident with the stellar components, with line-of-sight velocity offsets of a few hundred km s^{-1} . In Table 2, we list redshift and [O III] λ 5007 (hereafter [O III]) luminosity measurements for each individual nucleus from our ground-based long-slit spectroscopy.

3. OBSERVATIONS, DATA REDUCTION, AND ANALYSIS

3.1. *HST*/WFC3 *F336W* and *F105W* Imaging

The four optically selected kpc-scale binary AGNs were observed using the WFC3 on board the *HST* in Cycle 18 (program: GO 12363; PI: Shen). Each target was imaged in the UVIS/F336W (*U* band; Dressel 2010) and IR/F105W (wide *Y* band) filters within a single *HST* orbit. We refer to Paper II for details of our *HST* observations. Here, we briefly describe the data relevant for addressing the nature of the ionizing sources.

The *U*- and *Y*-band images were calibrated both photometrically and astrometrically. The typical relative astrometric

⁷ See also a fifth candidate, SDSS J1356+1026, reported by Shen et al. (2011a) and Greene et al. (2011, 2012).

Table 3
Nuclear U -band Fluxes and Luminosities, Extinction Estimates, and Inferred Star Formation Properties

Object Name	$\log f_U^{\text{obs}}$ (Jy)	$\log L_U^{\text{obs}}$ ($\text{erg s}^{-1} \text{ Hz}^{-1}$)	$\frac{F_{H\alpha}}{F_{H\beta}}$	$E(B - V)$ (mag)	A_U (mag)	$\log L_U$ ($\text{erg s}^{-1} \text{ Hz}^{-1}$)	SFR_U ($M_\odot \text{ yr}^{-1}$)	$L_{X,0.5-2\text{keV}}^{\text{SF}}$ ($10^{40} \text{ erg s}^{-1}$)	$L_{X,2-10\text{keV}}^{\text{SF}}$ ($10^{40} \text{ erg s}^{-1}$)
(1)	(2)	(3)	(4)	(5)	(6)	(7)	(8)	(9)	(10)
SDSS J1108+0659NW	-4.55	28.4	4.1	0.4	1.9 ± 0.7	29.2 ± 0.3	10	6	6
SDSS J1108+0659SE	<-5.93	<27.0	3.1	0.1	0.5 ± 0.8	<27.2 \pm 0.3	<0.1	<0.03	<0.03
SDSS J1131-0204W	<-5.97	<26.8	5.6	0.7	3.8 ± 0.3	<28.3 \pm 0.1	<1	<0.5	<0.6
SDSS J1131-0204E	-5.69	27.1	5.5	0.7	3.7 ± 0.4	28.5 ± 0.2	2	1	1
SDSS J1146+5110SW	-4.91	27.7	3.1	0.1	0.4 ± 0.1	27.9 ± 0.1	0.4	0.2	0.2
SDSS J1146+5110NE	-4.44	28.2	3.1	0.1	0.5 ± 0.1	28.4 ± 0.1	2	0.7	0.8
SDSS J1332+0606SW	-5.39	27.7	3.5	0.2	0.9 ± 0.3	28.1 ± 0.1	0.6	0.3	0.3
SDSS J1332+0606NE	-5.25	27.8	4.7	0.5	2.3 ± 0.9	28.8 ± 0.4	4	2	2

Notes. All measurements for each nucleus were made within the same aperture as for the X-ray extraction. Column 2: observed U -band flux density. Column 3: observed U -band luminosity density. Column 4: Balmer decrement measured from our ground-based slit spectra (Liu et al. 2010a). Column 5: color excess estimated from the Balmer decrement. Column 6: U -band extinction estimated from the Balmer decrement and uncertainty due to aperture coverage mismatch (see Section 4.2.1). Column 7: extinction-corrected U -band luminosity density and uncertainty (propagated from the extinction uncertainty due to aperture mismatch only, not including that due to uncertain dust geometry). Column 8: star formation rate inferred from the extinction-corrected U -band luminosity density (see Section 3.1 for details). Typical uncertainty is ~ 0.3 dex, which was estimated by convolving that propagated from L_U with the rms scatter of the SFR- L_U calibration (Equation (1)). Columns 9 and 10: X-ray luminosities inferred from the SFR estimate, assuming the empirical calibration of Ranalli et al. (2003, see Section 4.2 for details). Typical uncertainty is ~ 0.4 dex, which was estimated by convolving that propagated from SFR estimates with the rms scatter of the SFR- L_X calibrations (Equations (3) and (4)).

accuracy is $0''.004$ for the U -band and $0''.01$ for the Y -band images. To improve absolute astrometric accuracy and to compare with X-ray images, we have registered the U - and Y -band images with the SDSS astrometry. The resulting absolute astrometric uncertainties of the registered U - and Y -band images were estimated as $\sim 0''.25$ and $\sim 0''.20$, respectively (Paper II). We list the Y -band nuclear positions in Table 2 and the inferred separations between the double nuclei for each target in Table 1. These Y -band nuclear separations agree with those measured from our ground-based NIR imaging within uncertainties.

At the redshifts of our targets ($z = 0.130\text{--}0.207$; Table 1), the U -band filter covers rest-frame $\sim 2600\text{--}3200$ Å. For obscured AGNs, this wavelength range is likely to be dominated by continuum photospheric emission from host galaxy young stellar populations, which offers a useful indicator for the star formation rate (SFR; e.g., Cram et al. 1998). The U -band filter also covers line emission from ionized gas, although the contamination from even the strongest line, Mg II $\lambda 2800$, is likely insignificant ($< 1\%$), given that its typical equivalent width is small (e.g., 5.2 ± 0.8 Å, as measured from the composite spectrum of Type 2 AGNs by Zakamska et al. 2003). The U -band images may also contain AGN light from the obscured nuclei scattered into our line-of-sight by dust and/or gas (e.g., Zakamska et al. 2006), but our data suggest that the contribution is likely insignificant ($< 5\%$), because of the moderate AGN luminosities of our sample (Table 2) and the absence of a broad H β or H α component in the optical spectra (e.g., Liu et al. 2009). Finally, the U band could also contain nebular continua emitted by the ionized gas associated with the AGN emission-line region (Osterbrock 1989). Based on the observed fluxes and reddening estimates of the Balmer lines from our optical slit spectra (Liu et al. 2010a), we estimate that the nebular continua contribute to $\sim 5\%$ – 20% of the U -band flux at 2900 Å. Therefore, the nebular continua could make a considerable contamination to, but do not dominate, the observed U -band flux. The possible contamination from all of these non-star formation related processes would lower the estimated SFRs and strengthen the case of an AGN component.

Our high-resolution U -band imaging provides constraints on the intensity and spatial distribution of star formation activity in the host galaxies (Paper II). The inferred nuclear SFRs

are useful for estimating the X-ray contribution from star-formation-related processes (Section 4.2). In Table 3, we list the observed U -band flux f_U and luminosity L_U^{obs} integrated within a region centered on each Y -band nucleus position, with an aperture size matched to that of X-ray extraction (Sections 3.2.2 and 3.2.3). To estimate the intrinsic L_U , we have adopted an extinction correction for each nucleus (Table 3), based on the Balmer decrement $F_{H\alpha}/F_{H\beta}$ measured from our spatially resolved optical spectroscopy (Liu et al. 2010a). We assume the extinction curve of Cardelli et al. (1989) with $R_V = 3.1$ to calculate the Balmer decrement. We have carefully subtracted the host galaxy stellar continuum using population synthesis models (Bruzual & Charlot 2003) with the fitting method of Liu et al. (2009) in order to avoid overestimating the ratio $F_{H\alpha}/F_{H\beta}$ due to strong Balmer absorption in post-starburst populations. To estimate SFR from L_U , we have adopted the empirical calibration of Hopkins et al. (2003), which is given by

$$\frac{\text{SFR}_U}{M_\odot \text{ yr}^{-1}} = \left(\frac{L_U}{1.81 \times 10^{28} \text{ erg s}^{-1} \text{ Hz}^{-1}} \right)^{1.186}, \quad (1)$$

with an rms scatter of 0.13 dex. The relation was based on the SDSS u -band luminosity (corrected for obscuration) of 2625 star-forming galaxies in the SDSS DR1 (Abazajian et al. 2003), which was calibrated against SFR estimates inferred from H α emission-line measurements (corrected for aperture and obscuration effects) according to the relation of Kennicutt (1998); it is valid⁸ for $2 \times 10^{28} \text{ erg s}^{-1} \text{ Hz}^{-1} \lesssim L_U \lesssim 10^{30} \text{ erg s}^{-1} \text{ Hz}^{-1}$. Hopkins et al. (2003) have shown that the inferred SFR_U is consistent with SFR estimates from the 1.4 GHz luminosity (which was in turn calibrated from the FIR luminosity according to Kennicutt 1998; Bell 2003) with an rms scatter of 0.23 dex. Below, in Section 4.2.1, we discuss systematics and uncertainties in our SFR estimates, and by extension the inferred X-ray luminosity due to star-formation-related processes (Section 4.2).

⁸ For the three weakest U -band nuclei in our sample (Table 3), the L_U measurements are ~ 10 times lower than the faint luminosity end of the SDSS star-forming galaxy sample studied by Hopkins et al. (2003). To estimate SFRs for these faint nuclei, we assume the SFR- L_U relation by Hopkins et al. (2003) extrapolated to lower luminosities.

Table 4
X-Ray Properties and Spectral Models

Object Name	N_{H} (Galactic) (10^{20} cm^{-2})	Exposure (s)	T (counts)	S (counts)	H (counts)	HR	Γ	$N_{\text{H}}(\Gamma = 1.8)$ (10^{22} cm^{-2})
(1)	(2)	(3)	(4)	(5)	(6)	(7)	(8)	(9)
SDSS J1108+0659NW	3.99	19273	25.4 ± 5.0	20.5 ± 4.5	4.3 ± 2.1	$-0.60^{+0.11}_{-0.19}$	$2.4^{+0.6}_{-0.4}$	$<10^{-2}$
SDSS J1108+0659SE	3.99	19273	12.4 ± 3.5	2.5 ± 1.6	9.1 ± 3.0	$0.46^{+0.32}_{-0.16}$	$0.0^{+0.4}_{-0.6}$	3^{+3}_{-1}
SDSS J1131-0204W	3.34	23723	<6.6
SDSS J1131-0204E	3.34	23723	<6.6
SDSS J1146+5110SW	1.58	15432	16.6 ± 5.2	2.9 ± 2.9	13.6 ± 4.8	$0.65^{+0.19}_{-0.17}$	$-0.4^{+0.4}_{-0.5}$	4.0 ± 1.5
SDSS J1146+5110NE	1.58	15432	4.6 ± 3.4	4.6 ± 3.4	<1.8	<-0.81	>3.0	$<10^{-2}$
SDSS J1332+0606SW	2.21	23952	<10.9
SDSS J1332+0606NE	2.21	23952	7.7 ± 2.9	3.9 ± 3.2	3.7 ± 3.2	$-0.03^{+0.31}_{-0.36}$	$1.1^{+0.8}_{-0.7}$	$1.0^{+2.0}_{-0.99}$

Notes. Column 2: galactic column density, calculated adopting the neutral hydrogen data set compiled by Dickey & Lockman (1990), using the CIAO observing toolkit at <http://asc.harvard.edu/toolkit/colden.jsp>. Column 3: ACIS exposure time. Column 4: total 0.5–10 keV counts. Column 5: soft 0.5–2 keV counts. Column 6: hard 2–10 keV counts. Column 7: hardness ratio, $\text{HR} \equiv (H - S)/(H + S)$. Column 8: photon index of a power-law model where $n(E) \propto E^{-\Gamma}$, assuming Galactic column density. Column 9: intrinsic column density estimated assuming a power-law model with $\Gamma = 1.8$, a typical value for unobscured AGNs (e.g., Green et al. 2009), absorbed by a gas column N_{H} .

3.2. Chandra ACIS X-Ray Imaging Spectroscopy

The four kpc-scale binary-AGN candidates were observed with the ACIS-S on board the *Chandra X-ray Observatory* between 2011 February and November (Cycle 12 program: GO1-12127X; PI: Shen). Exposure times ranged from 16 ks to 24 ks (Table 4). They were set by the requirement of obtaining ~ 100 counts in the 0.5–10 keV from the weaker nucleus of each target. The counts were estimated from the [O III] luminosity for each nucleus, using the empirical correlation between 2–10 keV (unabsorbed) and [O III] luminosities (extinction corrected) from Panessa et al. (2006) as the baseline value, taking into account systematic uncertainties using the Heckman et al. (2005) relation (for observed luminosities) for optically selected single Type 2 AGNs, assuming a single power-law spectrum with an absorbing column density $N_{\text{H}} = 10^{23} \text{ cm}^{-2}$ (typical for Type 2 Seyferts; Bassani et al. 1999) and a photon index $\Gamma = 1.8$ (typical for unabsorbed Seyferts; Green et al. 2009). All of the targets were observed on-axis on the S3 chip, $9''$ to $15''$ away from the aimpoint. We examined the light curves and found no flares of either the sources or the background in each of the observations.

We reprocessed the data using the standard Chandra Interactive Analysis of Observations (CIAO) software (Fruscione et al. 2006) with version 4.4. We ran the `chandra_repro` script on the standard Level 2 event file for the recommended processing steps by the Chandra X-ray Center, applying the latest calibration files (CALDB 4.4.1). The process corrected for charge transfer inefficiency and time-dependent gain. The energy-dependent subpixel event repositioning (EDSER) algorithm (Li et al. 2004) was applied to improve the image quality of ACIS-S data for sources near the optical axis of the telescope, where the point spread function (PSF) is undersampled by the $0'.5$ ACIS pixels. Our targets have low count rates, so pileup effects (Ballet 1999) were insignificant.

3.2.1. Astrometric Uncertainty of ACIS Images

First, we discuss astrometry of ACIS images and our effort to obtain accurate alignment between the X-ray and optical images, which are important to determining the nature of X-ray sources. For sources within 3 arcmin of the aimpoint, the typical absolute

ACIS-S astrometric accuracy is $\lesssim 0'.6^9$ (radius size of the overall 90% uncertainty circle of ACIS-S absolute position; *Chandra* Proposers' Observatory Guide,¹⁰ hereafter POG). The relative astrometric accuracy is $0'.15$ (90% limit) for on-axis sources.¹¹

Astrometric calibration was applied as part of the pipeline processing of ACIS images. To verify the astrometric accuracy, we ran `wavdetect` (Freeman et al. 2002), which is a wavelet-based algorithm for spatial analysis of Poisson data, to detect sources as references for any fine alignment, if needed, between the ACIS images and the SDSS, to which our *Y*-band images have been registered. We used `mkpsfmap` to create observation-specific PSF map files instead of using the PSF table. We adopted a high-significance threshold (`sigthresh = 10-8`, corresponding to one spurious source in a $10^4 \times 10^4$ pixel map) to ensure robust source detection.

For SDSS J1108+0659 (SDSS J1131-0204), the astrometry of the ACIS image agrees with that of the SDSS within $0'.2$ ($0'.2$), based on three (six) SDSS-matched sources detected by *Chandra* within 2 arcmin (5 arcmin) of the aimpoint. For SDSS J1146+5110, only one bright X-ray source was detected in the field of view, 1.6 arcmin away from the aimpoint, whose ACIS and SDSS positions agree within $0'.2$. For SDSS J1332+0606, the astrometry of the ACIS image agrees with that of the SDSS within $0'.3$, based on four SDSS-matched sources detected within 3 arcmin of the aimpoint. Given these results, we do not apply any further astrometry correction for the ACIS images, because the agreement is already comparable to the SDSS astrometric accuracy.

Figure 1 shows the unsmoothed ACIS images of our four targets in the full (0.5–10 keV), soft (0.5–2 keV), and hard (2–10 keV) bands, respectively. Given the low count levels (Table 4), we do not apply any smoothing to avoid artifacts. As we will show in Section 4.4, our targets are significantly weaker hard X-ray emitters than those predicted from both the Panessa et al. (2006) and Heckman et al. (2005) relations

⁹ This was inferred based on measuring the distances between the *Chandra* X-ray source positions and corresponding optical/radio counterpart positions from the Tycho2 (with astrometric accuracy of ~ 25 mas; Høg et al. 2000) and ICRS (with astrometric accuracy of ~ 1 mas; Ma et al. 1998) catalogs.

¹⁰ <http://cxc.harvard.edu/proposer/POG/>; see also <http://cxc.harvard.edu/cal/ASPECT/celmon/>.

¹¹ Based on the 900 ks ACIS-I observation of the Orion Nebula; POG.

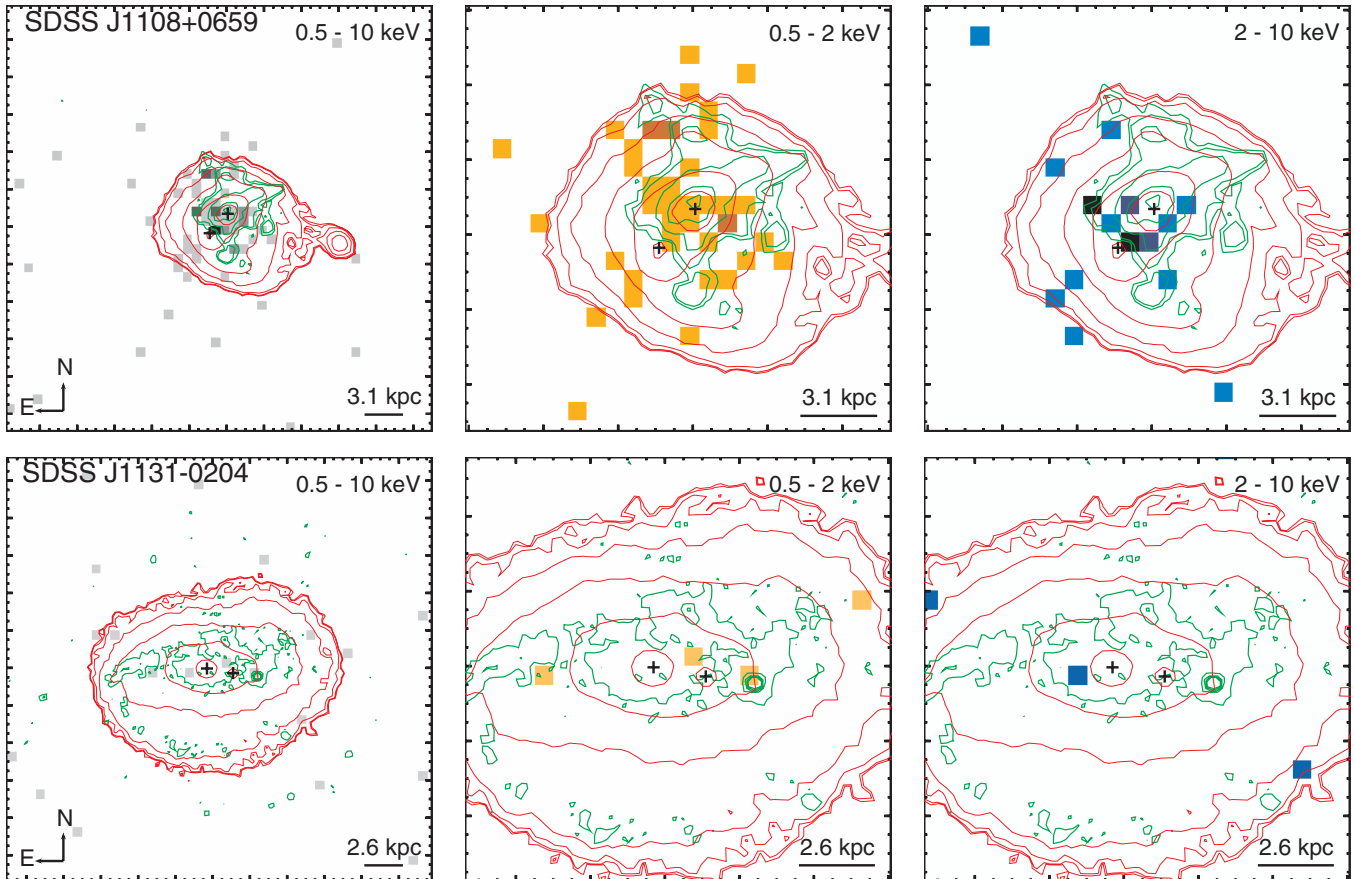


Figure 1. *Chandra* ACIS X-ray images ($0''.25$ pixel $^{-1}$ binning; unsmoothed) of the four optically selected kpc-scale binary AGNs. The left, middle, and right columns show the full band, and zoomed-in soft and hard bands, respectively. Contours are *HST*/WFC3 F105W (*Y* band; in red) and F336W (*U* band; in green) images in linear spacing. Black crosses indicate *Y*-band nuclear positions. Typical absolute (relative) astrometric uncertainty is $0''.20$ ($0''.15$) for our ACIS images (see Section 3.2.1 for details) and $0''.20$ ($0''.01$) for the *Y*-band images. Major tick marks are separated by $1''.0$.

(A color version of this figure is available in the online journal.)

for single optically selected AGNs (by $\sim 0.8 \pm 0.2$ dex and $\sim 1.9 \pm 0.3$ to 2.4 ± 0.3 dex in observed and unabsorbed 2–10 keV luminosities, respectively), resulting in far fewer counts than we expected. Five of the eight nuclei in our targets were detected in the full band (both nuclei in SDSS J1108+0659, both nuclei in SDSS J1146+5110, and the NE nucleus in SDSS J1332+0606), four of which were detected in both soft and hard bands (both nuclei in SDSS J1108+0659, the SW nucleus in SDSS J1146+5110, and the NE nucleus in SDSS J1332+0606), whereas one was only detected in the soft band (the NE nucleus in SDSS J1146+5110). The other three nuclei were undetected in the X-rays (both nuclei in SDSS J1131–0204, and the SW nucleus in SDSS J1332+0606).

Of the three X-ray detected targets, the *Y*-band nuclei in SDSS J1146+5110 and in SDSS J1332+0606 are separated by $1''.5$ and $2''.7$, respectively (Table 1), which are well within the resolving power of ACIS; the *Y*-band nuclei in SDSS J1108+0659 require more careful decomposition (Section 3.2.3). For the X-ray detected nuclei in SDSS J1146+5110 and SDSS J1332+0606, we compare their positions with the *Y*-band nuclear positions. We measure the X-ray position with a two-dimensional (2D) image fitting analysis using *Sherpa* (Freeman et al. 2001). We adopt a constant for the background and the PSF images as convolution kernels to fit the sources. We applied the *Y*-band positions as the initial guesses. PSF images were created

with the *MARX* software¹² using the PSF-ray table generated by the *Chandra* Ray Tracer (*ChaRT*; Carter et al. 2003), which simulates the best available PSF at any off-axis angle and for any energy or spectrum. As listed in Table 2, the X-ray positions agree with the *Y*-band positions within the uncertainties for all of the detected sources. We have compared the radial profile of our targets against PSF models. Each nucleus component is consistent with being an unresolved point source.

3.2.2. Source Extraction for Well-separated Nuclei

For SDSS J1146+5110 and SDSS J1332+0606, we run *dmextract* to extract X-ray counts for each individual nucleus. We use the positions and their uncertainties measured for each nucleus from the *HST* *Y*-band images as priors for source extraction. The background counts were extracted from source-free regions around the target regions. We report the number of background subtracted counts in separate soft (0.5–2 keV) and hard (2–10 keV) bands and in the full band in Table 4.

For each of the two nuclei in SDSS J1146+5110, we adopted a circular region with a $1''.2$ radius for source extraction. The adopted size ensured no overlap between the two sources, with each region containing more than 95% of the encircled energy (two-dimensional integral of the PSF). For SDSS J1332+0606, we extracted the counts for each nucleus in circular regions

¹² <http://space.mit.edu/ASC/MARX/index.html>

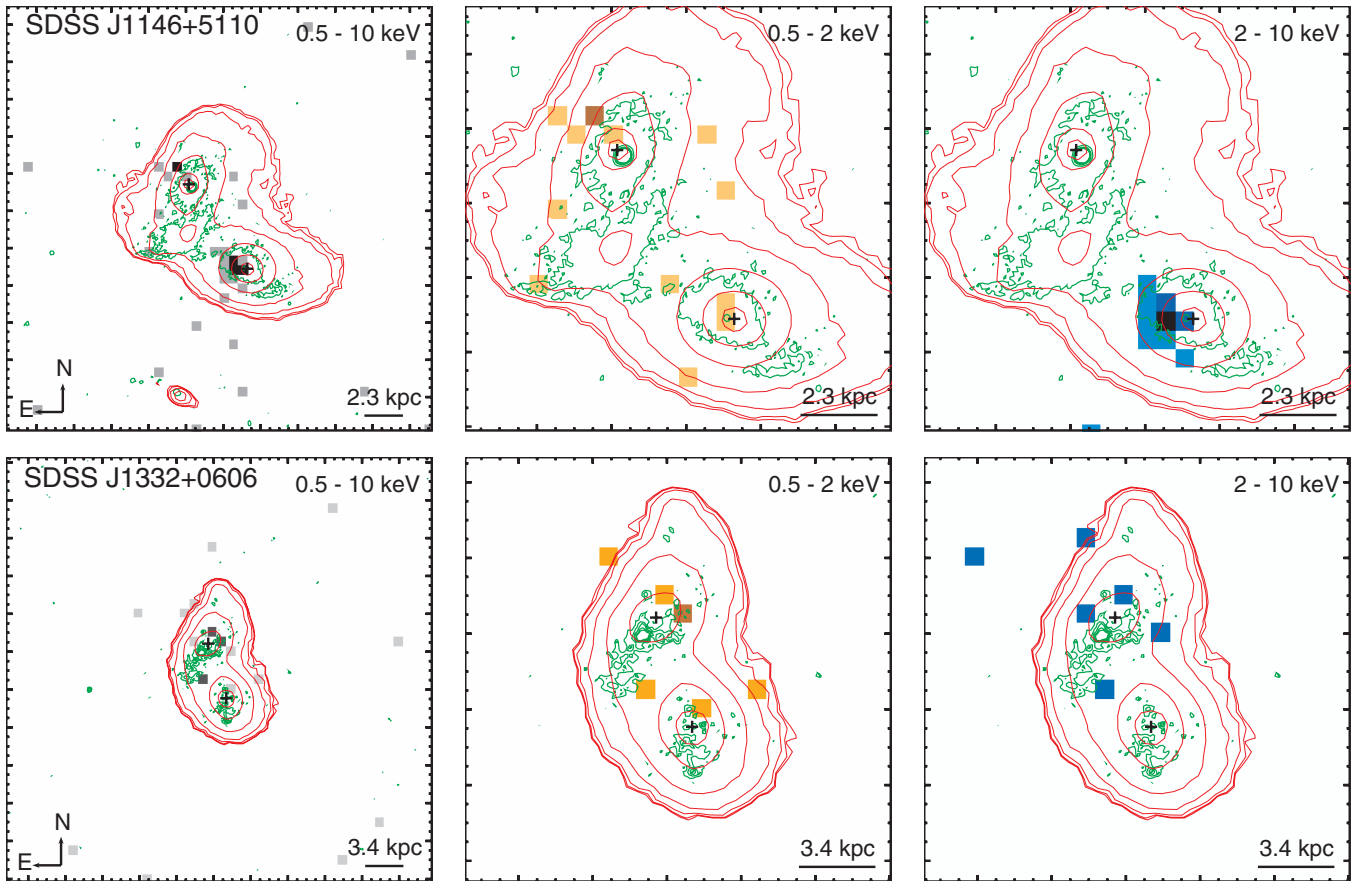


Figure 1. (Continued)

of $1''$ radii, to ensure that there was no overlap between the extraction regions of the two nuclei. No significant detection was obtained for the southern nucleus in SDSS J1332+0606; we estimated a 3σ upper limit according to the inferred background counts level using the tables in Gehrels (1986) appropriate for small numbers of events.

3.2.3. Source Decomposition for Marginally Resolved Nuclei

The Y -band nuclei of SDSS J1108+0659 and SDSS J1131–0204 are both separated by $0''.70$ (Table 1), which is close to the limit of the resolving power of ACIS. Neither one of the nuclei in SDSS J1131–0204 was detected in our observations, and we estimated a 3σ upper limit using the tables in Gehrels (1986) at the Y -band position of each nucleus.

To decompose the X-ray emission from the double nuclei in SDSS J1108+0659, we first performed a 2D image fitting in Sherpa, using PSF models as convolution kernels. We were unable to unambiguously separate the double nuclei, whose counts were too few for a statistically significant 2D decomposition. To increase the S/N, we then performed a one-dimensional (1D) analysis for the nuclear X-ray emission in SDSS J1108+0659, following the method used in Civano et al. (2012). There were too few counts to do a similar 1D analysis in SDSS J1131–0204.

For the 1D analysis in SDSS J1108+0659, we projected the X-ray (full-band) source profile in a direction connecting the two Y -band nuclei by extracting the counts in a grid of regions of $0''.5 \times 2''.0$, as shown in Figure 2. The grid was designed to minimize contamination from the extended emission to the northeast of the nuclear region. One caveat is that the apertures

used to derive the 1D profile may still contain emission from the extended structure, but we proceed by assuming that the emission within the nuclear apertures can be modeled as coming from a combination of point sources. We defer a full treatment of the properties and origins (e.g., starburst, shock heated gas, scattered AGN light, outflows and/or gas clouds photoionized by the AGN; Young et al. 2001; Evans et al. 2006) of the northeast extended soft X-ray emission to Paper II. Figure 2 shows the projected 1D source profile. We compared the 1D profile with the 2D PSF model projected and convolved with the same grid. We performed fitting in Sherpa using χ^2 statistics with the Gehrels variance function (Gehrels 1986); we tested two scenarios using one-component and two-component (i.e., two AGNs) PSF models, respectively. Centroids and amplitudes of the PSF models have been left free to vary. A likelihood ratio test suggests that the data marginally favor a two-component over a one-component model at the $\sim 1.5\sigma$ significance level.

We show in Figure 2 our best-fit model for the 1D nuclear source profile of SDSS J1108+0659. The best-fit central positions of the two sources are consistent (within 1σ uncertainties, $0''.2$) with the Y -band positions projected on the axis connecting the two nuclei. We report the best-fit X-ray nuclear positions of SDSS J1108+0659 in Table 2. We then repeated the decomposition analysis for the soft and hard bands, respectively. With fewer counts in the individual band fittings, we fixed the centroids of the two models at the best-fit positions from the full-band analysis, allowing only their amplitudes to vary. Figure 3 displays the best-fit models for the soft and hard band, respectively. The NW component is stronger (weaker) than the SE component in the soft (hard) band. The spectral properties

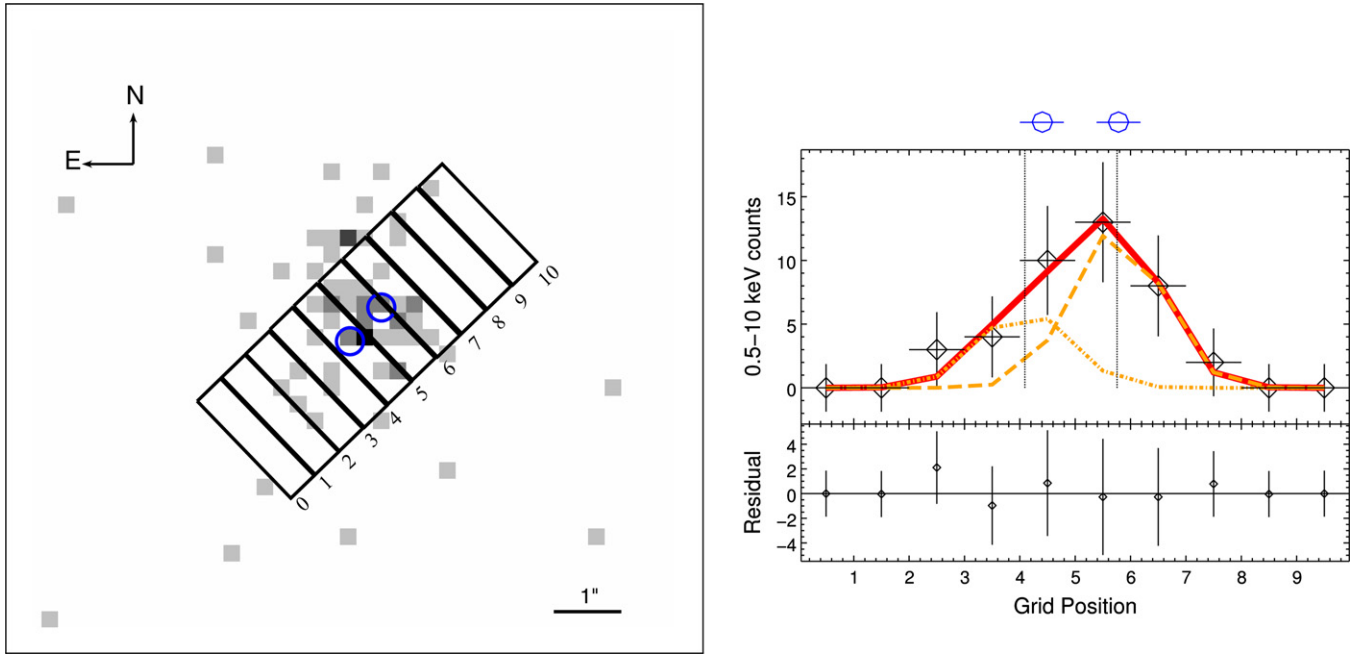


Figure 2. Left panel: the grid region for constructing the 1D spatial profile for SDSS J1108+0659. Background is the *Chandra* ACIS X-ray full-band image (unsmoothed with $0''.25$ pixel $^{-1}$ binning). The blue circles indicate the Y-band positions and uncertainties of the double stellar nuclei from our *HST* WFC3 imaging. Right panel: projected 1D profile of the nuclear X-ray emission in the full band. The grid positions correspond to those as shown by the grid region in the left panel and are separated by $0''.5$ (major tick marks). Data are shown in diamonds with error bars, whereas our best-fit models are displayed in solid (for the total) and dotted/dashed (for each individual component) curves, respectively. The vertical lines indicate the X-ray centers of the two components. The blue circles on top indicate the projected Y-band positions of the double stellar nuclei.

(A color version of this figure is available in the online journal.)

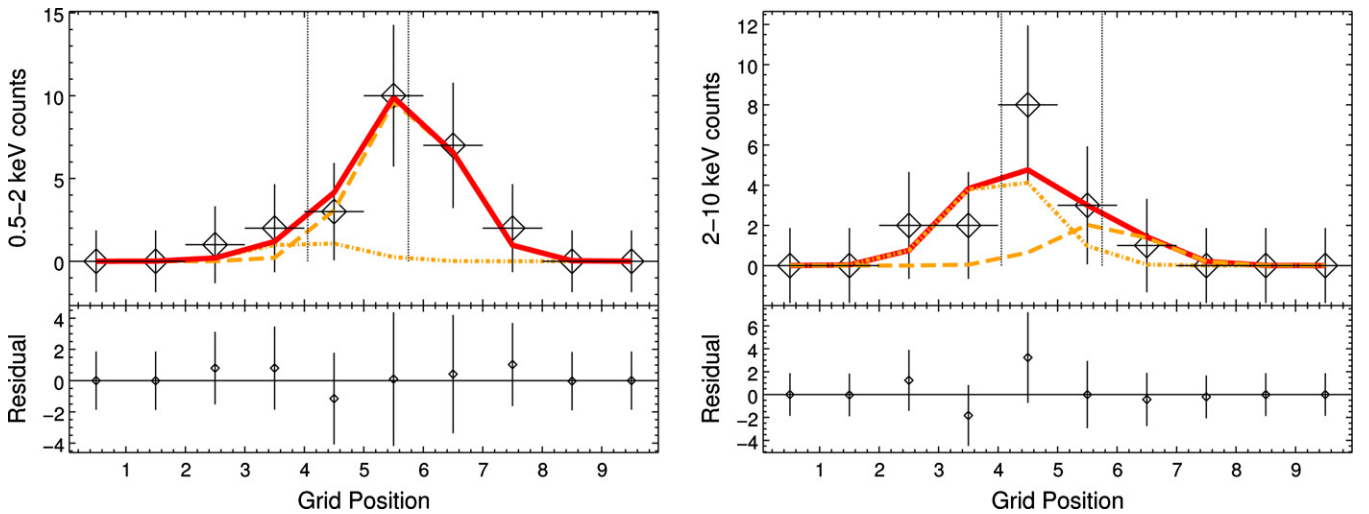


Figure 3. Same as in the right panel of Figure 2, but for the soft (left panel) and hard (right panel) band, respectively.

(A color version of this figure is available in the online journal.)

of the two sources seem to be significantly different from each other, lending further support to the two-component scenario. In Table 4, we report the number of background subtracted counts separately in the soft and hard bands as well as in the full band.

3.2.4. X-Ray Hardness Ratio and Spectral Analysis

There are too few X-ray counts of our targets to perform reliable spectral fitting. Instead, we estimate parameters of X-ray spectral models using hardness ratios (HR) as a proxy for detailed spectral fitting. The hardness ratio is defined as

$$\text{HR} \equiv \frac{H - S}{H + S}, \quad (2)$$

where H and S are the number of counts in the hard and soft bands, respectively. We adopted the Bayesian estimation of hardness ratios (Park et al. 2006) to measure the HRs and their uncertainties, appropriate for the low-count regime. To estimate the photon index Γ , we assume a single power-law model $n(E) \propto E^{-\Gamma}$, absorbed by the Galactic column density, calculated using the CIAO observing toolkit¹³ based on the neutral hydrogen data set compiled by Dickey & Lockman (1990). We also estimate the intrinsic galactic column density by fixing $\Gamma = 1.8$, typical for low-redshift unobscured Seyferts

¹³ <http://asc.harvard.edu/toolkit/colden.jsp>.

Table 5
X-Ray Fluxes and Luminosities

Object Name	$F_{X,0.5-10\text{keV}}$ (10^{-14} erg s $^{-1}$ cm $^{-2}$)	$F_{X,0.5-2\text{keV}}$ (10^{-14} erg s $^{-1}$ cm $^{-2}$)	$F_{X,2-10\text{keV}}$ (10^{-14} erg s $^{-1}$ cm $^{-2}$)	$L_{X,0.5-10\text{keV}}$ (10^{42} erg s $^{-1}$)	$L_{X,0.5-2\text{keV}}$ (10^{42} erg s $^{-1}$)	$L_{X,2-10\text{keV}}$ (10^{42} erg s $^{-1}$)
(1)	(2)	(3)	(4)	(5)	(6)	(7)
SDSS J1108+0659NW	1.05 ± 0.15	0.41 ± 0.08	0.46 ± 0.23	0.91 ± 0.17	0.34 ± 0.06	0.40 ± 0.20
SDSS J1108+0659SE (observed)	1.20 ± 0.35	0.054 ± 0.030	1.11 ± 0.36	1.08 ± 0.31	0.049 ± 0.032	1.00 ± 0.29
SDSS J1108+0659SE (unabsorbed)	2.10 ± 0.48	0.59 ± 0.38	1.31 ± 0.43	1.89 ± 0.53	0.53 ± 0.35	1.18 ± 0.42
SDSS J1131-0204W	<0.23	<0.1
SDSS J1131-0204E	<0.23	<0.1
SDSS J1146+5110SW (observed)	2.49 ± 0.78	0.08 ± 0.07	2.29 ± 0.81	1.05 ± 0.33	0.030 ± 0.025	0.96 ± 0.34
SDSS J1146+5110SW (unabsorbed)	5.2 ± 1.6	2.18 ± 0.77	3.2 ± 1.1	2.20 ± 0.69	0.92 ± 0.28	1.30 ± 0.46
SDSS J1146+5110NE	0.23 ± 0.17	0.23 ± 0.17	<0.9	0.10 ± 0.07	0.10 ± 0.07	<0.30
SDSS J1332+0606SW	<0.35	<0.37
SDSS J1332+0606NE (observed)	0.39 ± 0.14	0.062 ± 0.050	0.33 ± 0.28	0.43 ± 0.16	0.069 ± 0.057	0.37 ± 0.30
SDSS J1332+0606NE (unabsorbed)	0.56 ± 0.21	0.21 ± 0.16	0.35 ± 0.30	0.65 ± 0.24	0.23 ± 0.19	0.39 ± 0.31

Notes. Columns 2–4: total, soft, and hard X-ray flux and 1σ error. Columns 5–7: total, soft, and hard X-ray luminosity and 1σ error. For obscured sources, both observed (obs) and unabsorbed (unabs) estimates are listed. The unabsorbed estimates were calculated assuming a power-law model with $\Gamma = 1.8$ and N_{H} as derived from the HR measurements, as listed in Table 4. All errors quoted are statistical uncertainties only.

(e.g., Nandra & Pounds 1994; Green et al. 2009). We list in Table 4 our X-ray count measurements and estimates for model parameters for each detected nucleus.

We caution that the adopted single absorbed power-law model is most likely too simple for the X-ray spectra of obscured AGNs, in which thermal emission from starburst components and scattered nuclear emission is often present (e.g., Turner et al. 1997a, 1997b). However, the low counts of our detections do not allow us to test more realistic models. In addition, our estimates of the intrinsic absorbing column may not necessarily reflect the true values in cases of patchy obscuration and/or significant scattering off of an ionized medium in Compton-thick (i.e., $N_{\text{H}} \sim 10^{24}$ cm $^{-2}$ or larger) AGNs (which represent about half of the local Type 2 Seyfert population; Risaliti et al. 1999), as observed in NGC 6240 (e.g., Vignati et al. 1999; Ptak et al. 2003) and in NGC 1068 (e.g., Matt et al. 1997; Guainazzi et al. 1999), although, again, the quality of our data does not allow us to robustly test these possibilities.

4. RESULTS

We examine the nature of the ionizing sources in the four optically selected kpc-scale binary AGNs. We first discuss the intrinsic X-ray luminosity and spectral properties (Section 4.1). We then estimate the contribution from star-formation-related processes in the nuclear region to the observed X-ray flux (Section 4.2). Finally, we address whether these new X-ray and *HST* observations support the binary-AGN scenario for each target (Section 4.3), estimate the X-ray-to-[O III] luminosity ratio of optical kpc binary AGNs, and compare with single AGNs (Section 4.4).

4.1. X-Ray Luminosity and Spectral Properties

X-ray emission provides the most direct evidence for nuclear activity. In particular, the 2–10 keV hard X-ray band is transparent to column densities of $N_{\text{H}} \lesssim 10^{24}$ cm $^{-2}$. To infer X-ray luminosity, we assume a simple absorbed power-law model, with a fixed $\Gamma = 1.8$ and the estimated intrinsic host galaxy column density as given in Table 4. In Table 5, we list the observed X-ray flux and luminosity as well as the estimated unabsorbed/intrinsic X-ray luminosity of each nucleus in the total, soft, and hard bands, respectively.

The nuclei of our targets are optically classified as Type 2 AGNs (Liu et al. 2010a), whose observed [O III] luminosities (Table 2) suggest moderate AGN luminosities. The four hard X-ray detected nuclei have estimated unabsorbed 2–10 keV luminosities ranging from $(3.9 \pm 3.1) \times 10^{41}$ erg s $^{-1}$ to $(1.3 \pm 0.5) \times 10^{42}$ erg s $^{-1}$, and unabsorbed 0.5–10 keV luminosities ranging from $(6.5 \pm 2.4) \times 10^{41}$ erg s $^{-1}$ to $(2.2 \pm 0.7) \times 10^{42}$ erg s $^{-1}$. The estimated upper limits for the four hard X-ray undetected nuclei range from ~ 1.0 to 3.7×10^{41} erg s $^{-1}$ in 0.5–10 keV. These luminosity estimates are similar to the few previously known X-ray confirmed kpc-scale binary AGNs (NGC 6240, Komossa et al. 2003; 3C 75, Hudson et al. 2006; Mrk 463, Bianchi et al. 2008; Mrk 266, Brassington et al. 2007; and Mrk 739, Koss et al. 2011; see also Ballo et al. 2004 for a candidate Arp 299). We devote the rest of the section to determining the nature of the X-ray sources.

First, we consider the possibility of ultra-luminous X-ray sources (ULXs; with typical X-ray luminosities of the order of 10^{39} – 10^{40} erg s $^{-1}$, i.e., beyond high-mass X-ray binaries but much less than typical AGNs; Long & van Speybroeck 1983; Fabbiano 2006), which are off-nuclear point-like X-ray sources commonly observed in local major mergers of disk galaxies such as in Arp 244 (i.e., the Antennae) and Arp 270 (e.g., Brassington et al. 2007). Some ULXs may be accreting intermediate mass BHs ($M_{\text{BH}} \sim 10^2$ – $10^4 M_{\odot}$; e.g., Miller et al. 2003; Miller & Colbert 2004). Since the nuclei in our targets have X-ray luminosities much higher than typical ULXs, they are most likely of a different origin. Further evidence against the ULX scenario includes: (1) the BHs are expected to be supermassive given their host bulge properties (Liu et al. 2010a); (2) the observed [O III] luminosities are significantly higher than those for ULXs (Abolmasov et al. 2007); and (3) the X-ray point sources in our targets are nuclear given astrometric uncertainties, although ULXs could also live close to nuclear regions.

Second, the estimated intrinsic hard X-ray luminosities of our targets are close to or below $\sim 10^{42}$ erg s $^{-1}$ —the characteristic upper limit for the most luminous star-forming galaxies (e.g., Zezas et al. 2001). So it is quite possible that much or all of the luminosity is due to star formation. While X-ray spectral shape offers another diagnostic to discriminate between AGN and starburst scenarios, the uncertainties of our spectral estimates are too large to draw firm conclusions for the majority of the nuclei. Therefore, we must factor in some independent

SFR estimates to critically test the AGN scenario for each nucleus.

4.2. Contribution from Nuclear Star Formation

Even without the presence of an AGN, star-formation-related processes (e.g., accretion onto a neutron star or a BH in X-ray binaries, thermal bremsstrahlung from a starburst-driven wind; e.g., Strickland & Stevens 2000) may produce strong soft and hard X-ray emission. Intense nuclear star formation often accompanies and sometimes outshines AGNs in X-rays in gas-rich mergers, making kpc-scale binary AGNs challenging to pin down. To break the degeneracy, we first examine the contribution from nuclear star formation, using independent constraints from *HST* *U*-band imaging.

We estimate the expected X-ray emission due to star formation within the same apertures used to perform our X-ray extraction in order to evaluate if an additional ionizing source, i.e., an AGN component, is needed. To derive X-ray luminosities from SFRs, we adopt the empirical calibration of Ranalli et al. (2003, see also Grimm et al. 2003), based on 23 nearby star-forming galaxies, which is given by

$$L_{0.5-2\text{keV}}^{\text{SF}} = 4.5 \times 10^{39} \frac{\text{SFR}}{M_{\odot} \text{ yr}^{-1}} \text{ erg s}^{-1}, \quad (3)$$

$$L_{2-10\text{keV}}^{\text{SF}} = 5.0 \times 10^{39} \frac{\text{SFR}}{M_{\odot} \text{ yr}^{-1}} \text{ erg s}^{-1}, \quad (4)$$

with an rms scatter of 0.27 dex and 0.29 dex, respectively. In Table 3, we list the derived $L_{0.5-2\text{keV}}^{\text{SF}}$ and $L_{2-10\text{keV}}^{\text{SF}}$ estimates for each nucleus. The predicted X-ray contribution from star formation is an order of magnitude or more below the observed X-ray luminosity. At this point, the case that the X-rays are coming from AGN seems unambiguous, before considering the uncertainties.

4.2.1. Uncertainties

In this section, we discuss the systematics and uncertainties of our estimates of the expected X-ray luminosity due to star-formation-related processes. First, a Salpeter initial mass function (IMF; Salpeter 1955) was assumed with mass limits of $0.1 M_{\odot}$ and $100 M_{\odot}$ in the adopted calibration of SFR from *U*-band luminosity. The adopted SFR–X-ray-luminosity relation of Ranalli et al. (2003) was calibrated under the same assumptions for the IMF and mass range (essentially all from Kennicutt 1998), so that the inferred star-formation-related X-ray luminosity is not sensitive to the IMF uncertainty, given that there are no large systematic IMF variations among star-forming galaxies (Scalo 1986; Kroupa 2001; Chabrier 2003).

The uncertainty of the estimated X-ray luminosity due to star formation is likely to be dominated by the poorly constrained *U*-band extinction correction. First, we estimated $F_{\text{H}\alpha}/F_{\text{H}\beta}$ using emission-line measurements for each nucleus from our ground-based optical long-slit spectroscopy. Due to its lower angular resolution and projection effects, the aperture of the emission-line measurement does not exactly match with the *U*-band measurement. To estimate the reddening uncertainty due to this coverage mismatch, we have compared the emission-line ratio measurement from our slit spectroscopy against that from the SDSS fiber spectra. For the SDSS fiber-integrated measurements, we assumed that the two velocity components correspond to the two nucleus components, although the actual association is likely to be more complicated. Nevertheless, we

found that the uncertainty in *U*-band extinction estimates due to aperture mismatch is in general <1 mag (Table 3). Multi-color imaging and/or integral field unit spectroscopy with the same angular resolution as the *U*-band imaging would help to further constrain the uncertainty.

More importantly, the color excesses we derived using the Balmer decrement method do not necessarily represent the true dust content of our targets. For example, most of the dust could be concentrated on scales smaller than where the Balmer lines are emitted. High extinction with little reddening could arise in objects with very patchy and optically thick dust clouds. These caveats associated with the uncertainties in the extinction geometry and the reddening assumptions are typical, but must be kept in mind when extinction corrections are applied to compare with other studies in the literature.

4.3. Nature of the Ionizing Sources

In Figure 4, we compare the expected X-ray luminosities due to star formation against the observed X-ray luminosities in the soft and hard bands, respectively. Armed with both the observed X-ray properties and independent constraints on the expected X-ray contribution due to star formation from *U*-band imaging, we now discuss whether the observations support the binary-AGN scenario for each of our targets.

4.3.1. SDSS J1108+0659

Both nuclei were optically classified as Type 2 Seyferts, suggesting the presence of at least one AGN component. Both nuclei were detected in both soft and hard X-ray bands. The *U*-band image reveals intense star formation activity in the NW nuclear region. While the X-ray HR and Γ estimates (based on the simple absorbed power-law model) suggest no nuclear obscuration, the strong starburst component may be accompanied by significant dust and gas, suggesting the presence of a substantial absorbing column. The adopted single absorbed power-law model is most likely too simple, but there are too few X-ray counts to test more realistic multi-component spectral models. The spectral properties of the SE source suggest moderate nuclear obscuration, with an estimated column density of $N_{\text{H}} \sim 3_{-1}^{+3} \times 10^{22} \text{ cm}^{-2}$. The SE nucleus was undetected in the *U* band, indicating a very low level of star formation around the SE nucleus (or that the star formation was highly obscured). The spatial profiles of the two nuclear X-ray sources support the AGN scenarios for both, although the starburst components in the NW nucleus are too compact to be resolved in the X-rays. For both nuclei, the expected star-formation-related X-ray luminosities are too low (5.7 ± 1.0 times fainter in the soft and 6.7 ± 3.3 times fainter in the hard X-ray band for the NW nucleus, and at least three orders of magnitude fainter in both bands for the SE nucleus) to explain the observed values, lending further support to the binary-AGN scenario.

4.3.2. SDSS J1131–0204

Both nuclei were optically classified as Type 2 Seyferts, indicating that at least one AGN component must be present. Both nuclei were undetected in the two X-ray bands. The merger system seems to be embedded in a massive disk component, and we may be viewing the disk at an angle close to edge-on through a large amount of absorbing column. Our *U*-band image reveals circumnuclear star formation around the eastern nucleus, whereas the western nucleus was undetected in the *U* band. The *U*-band constraints on the expected star-formation-related

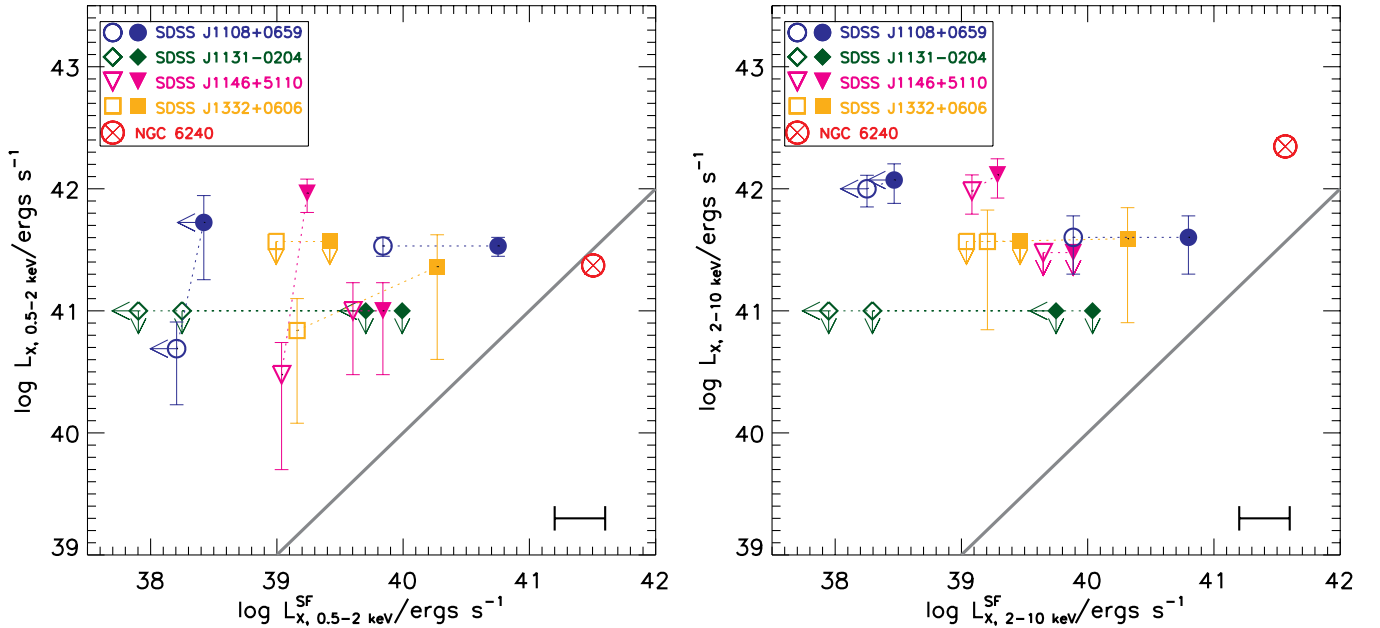


Figure 4. X-ray luminosities vs. the expected contribution from star-formation-related processes. We show the soft-band results in the left panel and the hard-band results in the right panel, respectively. Open symbols represent observed quantities, whereas filled symbols are corrected for dust extinction and gas absorption. We use dotted lines to connect values of the same nucleus before and after extinction/absorption correction. For comparison, we also show measurements of NGC 6240 (total emission from both nuclei) from the literature (Ptak et al. 2003). In both panels, we show the equality relation with a solid line. The error bar in the lower right of the panel indicates typical uncertainty (~ 0.4 dex) in the X-ray luminosity from star-formation-related processes, which was estimated by convolving that propagated from SFR estimates with the rms scatter of the SFR– L_X calibrations.

(A color version of this figure is available in the online journal.)

X-ray luminosities are still roughly an order of magnitude smaller than the observed X-ray luminosity upper limits for both nuclei. Therefore, the upper limits of the X-ray luminosities are still consistent with the presence of double AGNs, although the possibility that one AGN ionizes gas in both galaxies cannot be ruled out.

4.3.3. SDSS J1146+5110

The SW nucleus was optically classified as a Type 2 Seyfert, whereas the NE nucleus is either a Type 2 Seyfert, a LINER, or a LINER–H II composite. The X-ray spatial profiles of the two nuclei support the AGN scenario for both, although both nuclear starburst components are too compact to be resolved in the X-rays. The SW nucleus was detected in both soft and hard X-rays. Its HR and Γ measurements may suggest a mild obscuration ($N_H \sim 4.0 \pm 1.5 \times 10^{22} \text{ cm}^{-2}$ estimated assuming $\Gamma = 1.8$); its intrinsic hard X-ray luminosity ($L_{X,2-10 \text{ keV}} \sim 1.3 \pm 0.5 \times 10^{42} \text{ erg s}^{-1}$) is over two orders of magnitude larger than that expected from star formation (Figure 4), strongly suggesting an AGN component. The NE nucleus was detected only in the soft X-rays. Taken at face value, its HR and Γ estimates suggest a steep spectrum; this, together with its moderate hard X-ray luminosity ($L_{X,2-10 \text{ keV}} < 3.0 \times 10^{41} \text{ erg s}^{-1}$) may indicate a source dominated by star-formation-related processes. However, the expected star-formation-related X-ray luminosities are lower than the observed value (14 ± 10 times fainter in the soft band) or the upper limit (up to ~ 40 times fainter in the hard band), lending support for a low-luminosity AGN component also in the NE nucleus. Similar to the case of the NW nucleus of SDSS J1108+0659, the U -band image reveals intense star formation activity in the NE nuclear region of SDSS J1146+5110. While the apparent X-ray HR and Γ estimates suggest no significant absorbing column, the nuclear starburst component may indicate otherwise.

4.3.4. SDSS J1332+0606

Both nuclei were optically classified as Type 2 Seyferts. The NE nucleus was detected in both soft and hard X-rays, although the counts were very low. The apparent HR and Γ measurements may suggest a reflection dominated spectrum, indicating the presence of a Compton-thick source. In the Compton-thick scenario, the true intrinsic X-ray luminosities would be much higher than our fiducial estimates, where only modest absorption is assumed ($N_H \sim 1.0^{+2.0}_{-0.99} \times 10^{22} \text{ cm}^{-2}$ estimated assuming $\Gamma = 1.8$, i.e., consistent with zero absorption). The expected star-formation-related X-ray luminosities in both bands are lower than the observed values within the uncertainties, suggesting an AGN component. The SW nucleus was undetected in the X-rays. While the upper limits of the X-ray luminosities are consistent with an AGN component in the SW nucleus as well, the possibility that only one AGN in the NE nucleus ionizes gas in both galaxies cannot be ruled out.

In summary, our new *Chandra* and *HST* observations support the binary-AGN scenario for two of our four targets (SDSS J1108+0659 and SDSS J1146+5110). For the other two targets (SDSS J1131–0204 and SDSS J1332+0606), the existing data are still consistent with the binary-AGN scenario, although the possibility of only one AGN ionizing both components in the mergers cannot be fully ruled out.

4.4. X-Ray-to-[O III] Luminosity Ratio

For optically selected Type 2 AGNs, the [O III] emission-line luminosity is usually taken as a surrogate to estimate the intrinsic hard X-ray luminosity, because the intrinsic AGN continuum luminosity is obscured in the optical. Measurements of the ratio $L_{X,2-10 \text{ keV}}/L_{[\text{O III}]}$ for optically selected Type 2 AGNs span a wide range, with values ranging from a few to a few hundred

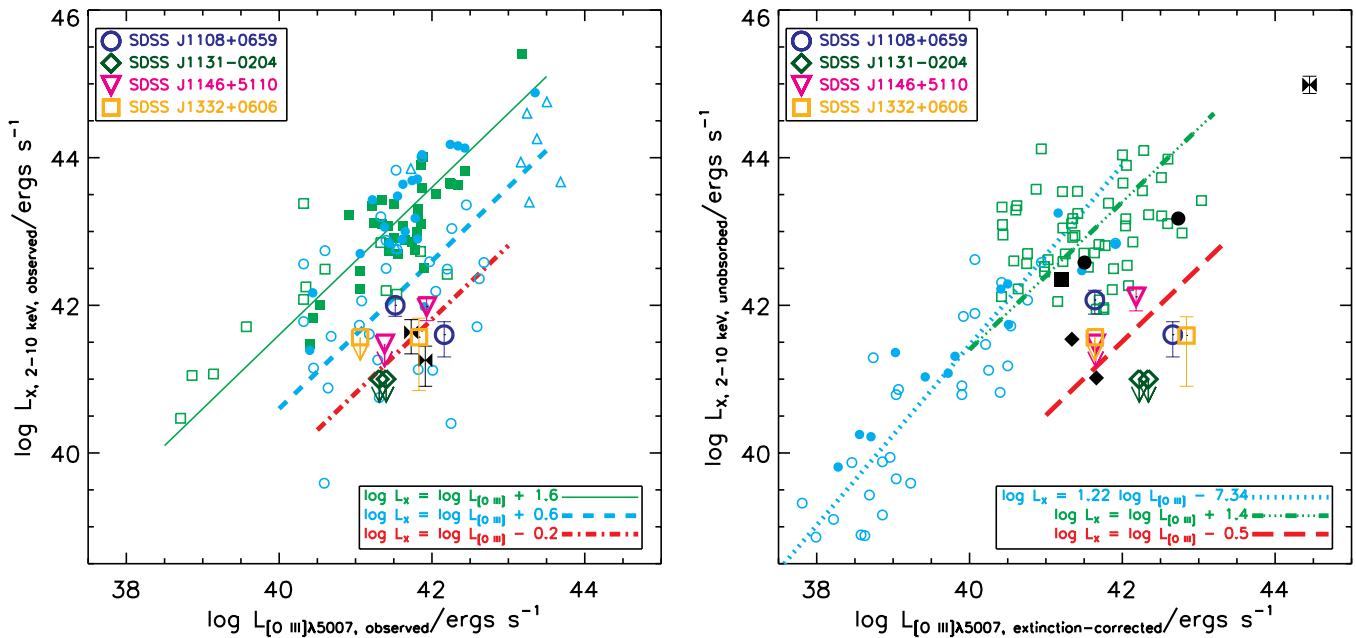


Figure 5. Hard X-ray vs. [O III] $\lambda 5007$ emission-line luminosity. Our targets are indicated with large colored open symbols, as denoted in the plot. Left panel: observed 2–10 keV luminosity vs. observed [O III] luminosity. The comparison samples include: hard X-ray selected AGNs (Type 1s as filled and Type 2s as open squares; both in green) and [O III] bright AGNs (Type 1s as filled and Type 2s as open circles; both in cyan) from Heckman et al. (2005), and optically selected Type 2 quasars (open upward triangles in cyan) from Ptak et al. (2006). The red dash-dotted line is the mean relation for our targets, the cyan dashed line is for optically selected Type 2 AGNs (Heckman et al. 2005), whereas the green solid line is for hard X-ray selected AGNs (both Type 1 and Type 2) and optically selected Type 1 AGNs (Heckman et al. 2005). Right panel: unabsorbed 2–10 keV luminosity vs. extinction-corrected [O III] luminosity. The comparison samples include: nearby optically selected Seyfert galaxies (Type 1 in filled and Type 2 in open circles; both in cyan) from Panessa et al. (2006), Type 2 Seyferts (green open squares) from the CSC-SDSS cross-match catalog of Trichas et al. (2012), and three previously known kpc-scale binary AGNs (NGC 6240 (a large filled square for the total nuclear emission; Ptak et al. 2003) from Komossa et al. 2003; Mrk 463 (large filled circles) from Mazzarella & Boroson 1993 and Bianchi et al. 2008; and Mrk 266 (large filled diamonds) from Brassington et al. 2007). The red long-dash line is the mean relation of our targets, the green dash-dot-dot line is for the CSC-SDSS sample, whereas the cyan dotted line is that from Panessa et al. (2006) for mixed Seyferts in nearby galaxies. Shown as filled bowties are two NLR-kinematics-candidate double-peaked [O III] AGNs (left panel: SDSS J1715+6008 from Comerford et al. 2011; and right panel: CXO J1426+35 (total emission) from Barrows et al. 2012).

(A color version of this figure is available in the online journal.)

(Mulchaey et al. 1994; Heckman et al. 2005; Panessa et al. 2006).

4.4.1. Systematically Smaller X-Ray-to-[O III] Luminosity Ratio in Optically Selected kpc-scale Binaries than in Single AGNs

In Figure 5, we plot the hard X-ray luminosity against the [O III] luminosity for each nucleus in our targets. For context, we compare our targets to observations of single AGNs and the few previously known kpc-scale binary AGNs. We study both the relation between the observed hard X-ray luminosity $L_{X,2-10\text{keV,observed}}$ and the observed [O III] luminosity $L_{[\text{O III}],\text{observed}}$, and that between the unabsorbed hard X-ray luminosity $L_{X,2-10\text{keV,unabsorbed}}$ and the extinction-corrected [O III] luminosity $L_{[\text{O III}],\text{extinction-corrected}}$. We used different comparison samples for the two as usually only the observed or the corrected luminosity was available in any given sample.

For the $L_{X,2-10\text{keV,observed}}-L_{[\text{O III}],\text{observed}}$ relation (left panel of Figure 5), the comparison samples include the 47 hard X-ray (3–20 keV, in this particular case) selected AGNs (the $z < 0.2$ subset of the Sazonov & Revnivtsev 2004 sample from the *RXTE* all sky survey; Revnivtsev et al. 2004), 55 optically selected local [O III]-bright AGNs (Xu et al. 1999; Whittle 1992) studied by Heckman et al. (2005), and 8 optically selected Type 2 quasars from Ptak et al. (2006). The Heckman et al. (2005) local AGN samples have similar redshifts and $L_{[\text{O III}],\text{observed}}$ to our targets, whereas the Ptak et al. (2006) objects are at higher redshifts ($z \sim 0.3-0.8$ compared to our targets at $z \sim 0.1-0.2$) and have higher $L_{[\text{O III}],\text{observed}}$ (by ~ 1.5 dex). Heckman

et al. (2005) showed that optically selected Type 2 AGNs have systematically lower $L_{X,2-10\text{keV,observed}}$ (by an average of 1.0 dex) at a given $L_{[\text{O III}],\text{observed}}$ than hard X-ray selected AGNs (both Type 1 and Type 2) and optically selected Type 1 AGNs. Our optically selected kpc-scale binary AGNs seem to have systematically smaller $L_X/L_{[\text{O III}]}$ (observed) values than even optically selected single Type 2 AGNs, although the sample size is still too small to draw a firm conclusion. The observed hard X-ray luminosities of our targets on average are $\sim 0.8 \pm 0.2$ dex smaller at least¹⁴ than those of optically selected single-nucleus Type 2 AGNs by Heckman et al. (2005) at a fixed $L_{[\text{O III}],\text{observed}}$ (i.e., average $\log(L_X/L_{[\text{O III}]}) = -0.2$ with an rms scatter of 0.40 dex, compared to $\log(L_X/L_{[\text{O III}]}) = 0.6$ with an rms scatter of 1.1 dex for optically selected single Type 2s).

For the $L_{X,2-10\text{keV,unabsorbed}}-L_{[\text{O III}],\text{extinction-corrected}}$ relation (right panel of Figure 5), the comparison samples include 47 Palomar Seyfert galaxies (optically selected Type 1 and Type 2 Seyferts drawn from the Palomar survey of nearby galaxies by Ho et al. 1995) from Panessa et al. (2006), and three previously known kpc-scale binary AGNs (NGC 6240 from Komossa et al. 2003 and Ptak et al. 2003; Mrk 463 from Bianchi et al. 2008; and Mrk 266 from Brassington et al. 2007). We also include a new sample of 55 single-nucleus Type 2 Seyferts from Trichas et al. (2012). This comparison sample was both optically and X-ray selected, and was constructed by cross-matching the Chandra Source Catalog (CSC; Evans et al. 2010) Release 1.1 with the

¹⁴ The upper limits were included in the fit as detections.

SDSS DR7 spectroscopic galaxy catalog at $z < 0.3$, and selecting objects whose optical emission-line ratios $[\text{O III}] \lambda 5007 / \text{H}\beta$ and $[\text{N II}] \lambda 6584 / \text{H}\alpha$ are characteristic of Type 2 Seyferts according to the Kewley et al. (2001) criteria.

Panessa et al. (2006) suggested that after properly accounting for absorption correction (including for Compton-thick sources), optically selected Type 1 and Type 2 Seyferts all follow the same $L_{X,2-10\text{keV,unabsorbed}} - L_{[\text{O III}],\text{extinction-corrected}}$ relation. In particular, optically selected Type 2 Seyferts, which were significantly X-ray weaker than Type 1 Seyferts and quasars, also obey the same relation, after the ‘‘Compton-thick’’ luminosity correction. The average absorption correction for Compton-thick sources (30% of the sample) is $\sim 2\text{--}3$ dex, or $\sim 0.5\text{--}1$ dex for the other Type 2 Seyferts. Their absorption correction, however, is significantly larger than that for our targets, although our correction may have been underestimated given the poor X-ray constraints.

After correction for gas absorption and dust extinction, the unabsorbed hard X-ray luminosities of our targets appear to be $\sim 2.4 \pm 0.3$ dex smaller (at $\log L_{[\text{O III}]}$ of 42.0) than those expected from the Panessa et al. (2006) relation, $\log L_X = 1.22 \log L_{[\text{O III}]} - 7.34$, although the absorption correction of our targets may have been significantly underestimated (Section 3.2.4). Our targets have average unabsorbed $\log(L_X/L_{[\text{O III}]}) = -0.5$ (with an rms scatter of 0.69 dex), which is $\sim 1.9 \pm 0.3$ dex lower than that of the CSC-SDSS cross-match comparison sample (average $\log(L_X/L_{[\text{O III}]}) = 1.4$ with an rms scatter of 0.77 dex). Like our targets, the three previously known kpc-scale binary AGNs (all of which are ULIRGs and were discovered in the X-rays) also show smaller unabsorbed $\log(L_X/L_{[\text{O III}]})$ values than the Panessa et al. (2006) relation.

4.4.2. Interpretation: Higher Nuclear Gas Concentration and/or Viewing Angle Effect

We now discuss possible causes of the apparent hard X-ray weak tendency in optically selected kpc-scale binary AGNs compared to optically selected single Type 2 AGNs. Simulations suggest that galaxy mergers may funnel a significant amount of gas toward galaxy centers, triggering both global and nuclear starburst activity as well as AGN (e.g., Hernquist 1989; Hopkins et al. 2008). Using a sample of 1286 AGN pairs spectroscopically selected from the SDSS with projected separations of a few kpc to a few tens of kpc (Liu et al. 2011), Liu et al. (2012b) have shown that the fraction of both single and double AGNs stays constant with decreasing projected separation at >20 kpc scales. This suggests that at wide separations, the majority of the observed AGNs are most likely due to stochastic accretion not associated with tidal interactions (e.g., Ciotti & Ostriker 2007; Ciotti et al. 2010). However, the fraction of both single and binary AGNs increases rapidly on scales below 20 kpc, indicating tidally enhanced AGN in close galaxy pairs (see also Ellison et al. 2011). In addition, the fraction of binary AGNs in close galaxy pairs is significantly higher than what would be expected from the random pairing of single AGNs. Together with the correlation observed in AGN luminosity between the merging components in a pair (Liu et al. 2012b), this provides direct evidence that the double AGN observed in close galaxy pairs may indeed be connected to merger activity. It is likely that the gas in kpc-scale binary AGNs is being tidally funneled all the way to the nuclear regions of both components, and it either fuels the binary AGN directly, or fuels a nuclear starburst which in turn feeds the BHs.

We therefore suggest that a higher gas column in the nuclear regions of kpc-scale binary AGNs, which is likely induced by the merger events, may be at the root of the observed X-ray weak tendency. Unlike X-ray emission that comes from the accretion disk/corona of the accreting SMBHs, $[\text{O III}]$ emission in the NLRs comes from much larger scales (Antonucci 1993; Urry & Padovani 1995), and should therefore be much less subject to nuclear obscuration. In this scenario, the X-ray absorption column was significantly underestimated for our targets, which is plausible given the large systematic uncertainty of our X-ray measurement. While the three previously known kpc-scale binary AGNs (which are all ULIRGs and whose binary-AGN nature was all discovered in the X-rays) also show smaller X-ray-to- $[\text{O III}]$ luminosity ratios than single Seyferts, the X-ray weak tendency seems to be less pronounced than for our optically selected kpc-scale binary AGNs. This may be due to either a selection effect, or a host-galaxy effect (i.e., the nuclear gas distribution in ULIRGs—disk-dominated mergers—is less concentrated than in optically selected binary AGNs—whose hosts have prominent stellar bulges—due to lower bulge-to-disk ratios of the host galaxies), or a combination of both.

Alternatively, the X-ray weak tendency observed in our targets may be caused by a viewing angle effect related to its double-peak selection. The requirement of detecting well-separated $[\text{O III}]$ double peaks in velocity is likely to pick out edge-on systems, and therefore would be biased toward a higher absorbing gas column. For example, SDSS J1131–0204, the only one of our targets which was undetected in the X-rays, appears to show two stellar nuclei imbedded in a large edge-on disk (Liu et al. 2010a; Shen et al. 2011a). To check whether the double-peak selection causes the X-rays to be weak, we also examine two double-peaked $[\text{O III}]$ AGNs in the literature with available $[\text{O III}]$ and hard X-ray luminosity measurements (SDSS J1715+6008 from Liu et al. 2010b, Smith et al. 2010, and Comerford et al. 2011, and CXO J1426+35 from Barrows et al. 2012) whose emission-line profiles are more likely caused by complex NLR kinematics, i.e., not caused by kpc-scale binary AGNs. As shown in Figure 5, in both cases, the X-ray-to- $[\text{O III}]$ ratios are smaller than the Heckman et al. (2005) and Panessa et al. (2006) relations for the observed and corrected luminosities, respectively. While this comparison is based on only two objects, it may suggest that the hard X-ray weak tendency is related to a double-peak selection, regardless of whether there are two active BHs in the system. However, the viewing angle effect is unlikely to be the sole cause of the X-ray weak tendency, given that the three previously known kpc-scale binary AGNs, which were not selected from double-peaked narrow-line AGNs, also show smaller X-ray-to- $[\text{O III}]$ luminosity ratios than single Seyferts.

In summary, we conclude that the observed X-ray weak tendency in our optically selected kpc-scale binary AGNs is likely caused by a combination of (1) a higher nuclear gas column, which may be induced by merger events, and (2) a viewing angle bias related to its double-peak NEL selection. Of course, another possibility is that we were simply unlucky with these four systems, and they are not typical of kpc-scale binary AGNs.

5. DISCUSSION

We discuss the implications of our results for the general double-peak narrow-line selection approach of identifying kpc-scale binary AGNs (Section 5.1), for the attributes and limitations of optical identification compared to X-ray searches

(Section 5.2), and for the observed frequency of kpc-scale binary AGNs (Section 5.3).

5.1. On the Double-peak Approach for kpc-scale Binary-AGN Identification

5.1.1. X-Ray Confirmation of Optical Candidates: Success and Ambiguity

Until recently, searches for kpc-scale binary AGNs have been more or less serendipitous. Previous work (Liu et al. 2010a; McGurk et al. 2011; Shen et al. 2011a; Fu et al. 2012) has demonstrated that selecting candidates based on double-peaked NELs and follow-up with high spatial resolution imaging (Fu et al. 2011a; Rosario et al. 2011) and spatially resolved spectroscopy (Comerford et al. 2012) is a promising way to identify kpc-scale binary AGNs. With the new *Chandra* and *HST* observations presented here, we have critically examined the nature of the ionizing sources of the optically identified kpc-scale binary AGNs. Our results confirm the kpc-scale binary-AGN nature for two of the four optical candidates; the data are still consistent with the binary scenario for the other two, but we cannot rule out the possibility of one AGN ionizing gas in both merging components. While the result lends some further support to the overall approach of systematically identifying kpc-scale binary AGNs based on the double-peak selection, it also suggests that X-ray confirmation of optical binary candidates can be challenging and ambiguous, due to the complex nature of X-ray obscuring in mergers.

5.1.2. Importance of Identifying Double Nuclei Both in Gas and in Stars

Shen et al. (2011a, see also Fu et al. 2012) suggested that the majority of optically selected AGNs with double-peaked [O III] $\lambda\lambda 4959, 5007$ emission lines are not due to kpc-scale binary AGNs, but are caused by complex NLR gas kinematics around single AGNs, such as outflows (e.g., Rosario et al. 2010) and/or rotating disks (e.g., Smith et al. 2012; Blecha et al. 2012b). Shen et al. (2011a) combined high-resolution NIR imaging (to resolve the double stellar bulges and to detect tidal features) with spatially resolved optical spectroscopy (to locate the ionizing sources and to register with the BHs/bulges) to identify strong kpc binary-AGN candidates (see also McGurk et al. 2011). Detecting two stellar components alone (e.g., Fu et al. 2011a; Rosario et al. 2011) is not a sufficient condition for identifying binary AGNs, as the double-peaked profile could be caused by NLR gas kinematics around a single AGN in a merger. Nor is detecting spatial offsets between the emission-line components alone (e.g., Gerke et al. 2007; Comerford et al. 2009a; Barrows et al. 2012) a sufficient condition, even though most double-peaked AGNs show spatial offsets on kpc scales between the two velocity components (Shen et al. 2011a; Fu et al. 2012; Comerford et al. 2012), because such spatial offsets are also expected and commonly observed in single AGNs due to the spatial extent of the NLR, as demonstrated by Fischer et al. (2011) in Mrk 78 (see also Whittle & Wilson 2004).

We emphasize the importance of detecting double nuclei in both gas and stars in the identification of kpc-scale binary AGNs. To pin down the ionizing sources, candidates from spatially resolved optical spectroscopy can be confirmed using imaging spectroscopy in the X-rays (as in this work) or in the radio (Fu et al. 2011b). However, identifying the double stellar bulges should be a prerequisite before carrying out X-ray or radio observations. X-ray and/or radio observations

would help to clarify the ambiguities for gas (i.e., in [O III]), but cannot substitute deep NIR imaging for stars. Double X-ray and/or radio sources (as well as spatially resolved optical emission regions coincident with double X-ray/radio sources) on a smooth stellar background (e.g., see the candidate reported by Comerford et al. 2011) are more likely to be complex NLR gas kinematics (e.g., a jet; Comerford et al. 2011) rather than binary AGNs, as in the case of Mrk 78. Exceptions to this include binary AGNs with separations smaller than ~ 100 pc, where the two stellar bulges may have merged, and minor mergers, which are difficult to resolve due to large contrast ratios (see the candidate example discovered by Fabbiano et al. 2011).

5.1.3. Importance of High-resolution Deep Observations

Our new *Chandra* and *HST* observations have unambiguously confirmed the kpc-scale binary-AGN nature for SDSS J1108+0659 and SDSS J1146+5110. Fu et al. (2012) suggested that the case for SDSS J1108+0659 was ambiguous based on the detection of extended emission-line regions (EELRs) using Keck NIR imaging assisted with laser guide star AO and seeing-limited integral field spectroscopy (IFS) on the University of Hawaii 2.2 m telescope. However, the angular resolution of the IFS data (seeing $\sim 0''.8$) may have been insufficient to fully resolve the close double nuclei in SDSS J1108+0659 (angular separation of $0''.70$; Table 1). More importantly, the detection of EELRs on larger scales should not be taken as evidence for or against the binary-AGN scenario, because EELRs have been observed in both kpc-scale binary (such as in NGC 6240 and in Mrk 266) and single AGNs.

Fu et al. (2012) also suggested that SDSS J1146+5110 was a pair of EELRs powered by a single AGN, but their IFS data were not sensitive enough to detect the faint [O III] emission associated with the NE nucleus, which was detected by Liu et al. (2010a) using long-slit spectroscopy with the APO 3.5 m telescope.

5.2. Comparing Optical to X-Ray Identification of kpc-scale Binary AGNs

We discuss our results in the context of comparing optical and X-ray identification of kpc-scale binary AGNs. The identification of AGNs based on any particular wavelength window is likely to be limited by biases and incompleteness. For example, Heckman et al. (2005) suggested that identifying AGNs based on bright [O III] emission lines will uncover the majority of hard X-ray selected AGNs,¹⁵ whereas identifying AGNs by hard X-rays will miss a significant population of AGNs selected based on the [O III] optical emission line. These hard X-ray faint yet [O III] bright Type 2 AGNs are generally interpreted as heavily obscured or even Compton-thick sources (e.g., Risaliti et al. 1999; Bassani et al. 1999; Levenson et al. 2002).

Hard X-ray searches for kpc-scale binary AGNs are still limited by low angular resolution and small number statistics. Low-resolution studies (e.g., by Jiménez-Bailón et al. 2007 using the *XMM-Newton*; Jansen et al. 2001) are in general restricted to wide (tens of kpc scales) pairs in the local universe, whereas high-resolution searches with *Chandra* are often confined to relatively small samples (e.g., Teng et al. 2005, 2012). In addition, X-ray searches often have to apply some pre-selection based on optical AGN diagnostics to boost the success rate.

¹⁵ Except for BL Lac objects (Wolfe 1978) which contain very weak optical emission lines (Collinge et al. 2005).

Similar to heavily obscured single AGNs, our result for the hard-X-ray-to-[O III] luminosity ratio suggests that identifying kpc binary AGNs by hard X-rays is likely to miss a population of optically selected Type 2 binary AGNs. Addressing the fraction of such heavily X-ray-obscured binary AGNs among all binary AGNs would require knowledge of the space densities of Type-1–Type-1 and Type-1–Type-2 binaries, both optically selected and hard X-ray selected, which is beyond the scope of this paper. However, given our result that the hard-X-ray-to-[O III] $\lambda 5007$ luminosity ratio of optically selected Type 2 binary AGNs appears to be systematically smaller than single Type 2 AGNs, we speculate that the obscured fraction could be even higher in binary than in single AGNs.

On the other hand, Type 2 Seyferts were selected as the parent sample of double-peaked NEL AGNs (Liu et al. 2010b). By construction, this will miss Type 1 binary AGNs,¹⁶ mixed Type 1/Type 2, and Type 2 binaries involving LINERS and/or AGN–H II composites. In particular, the two nuclei of the prototypical kpc-scale binary AGN NGC 6240 (Komossa et al. 2003) are both heavily obscured in the optical, with emission-line ratios characteristic of LINERS (Lutz et al. 1999); another example is Mrk 266, whose northern nucleus is optically classified as a composite yet contains an X-ray AGN (Brassington et al. 2007; Mazzarella et al. 2012). Liu et al. (2011) have addressed the frequency of binary AGNs (including both Type 1 and Type 2 objects as well as LINERS and composites) on a few kpc to tens of kpc scales using spectroscopic galaxy pairs from the SDSS DR7. Complementary to the double-peak approach, the Liu et al. (2011) sample includes both Type 1 and Type 2 AGNs but is biased against binaries closer than 5 kpc in projection. While more work is clearly needed to address the frequency of kpc-scale Type 1 binaries and Type 2 binaries containing LINERS/composites, the frequency of kpc-scale binary AGNs inferred from the Liu et al. (2011) sample is similar to that from the double-peak approach (Liu et al. 2010a; Shen et al. 2011a), suggesting that the majority of kpc-scale binary AGNs are Type 2 objects, most of which are Seyferts, at least in the moderate AGN-luminosity regime being considered.

5.3. Frequency of kpc-scale Binary AGNs

Motivated by the serendipitous success in NGC 6240, Teng et al. (2005) carried out a systematic search for binary AGNs using *Chandra* imaging of a sample of eight (U)LIRGs that contain double stellar nuclei; they found no additional strong candidate. Similarly, Teng et al. (2012) carried out a *Chandra* survey of a sample of 12 massive galaxy mergers, each of which contains one optical AGN, but found no convincing case of binary AGNs. The null results from such “blind” X-ray searches in small samples are not unexpected, considering the relatively low frequency of kpc binary AGNs as measured using optical identification based on much larger parent samples (Liu et al. 2010a, 2011; Shen et al. 2011a; Fu et al. 2012). The kpc-scale binary-AGN fraction from optical studies (e.g., $\sim 0.5\%$ – 2.5% ; Shen et al. 2011a) is also consistent with the

X-ray estimate ($\sim 2\%$) by Koss et al. (2012), considering statistical and systematic uncertainties.

Using follow-up NIR imaging and optical slit spectroscopy of 43 double-peaked [O III] Type 2 AGNs from the parent sample presented in Liu et al. (2010b), Shen et al. (2011a) have estimated that $\sim 0.5\%$ – 2.5% of Type 2 AGNs at $z < 0.3$ are kpc-scale binary AGNs of comparable luminosities, with a relative orbital velocity of $\gtrsim 150$ km s⁻¹ (see also Liu et al. 2010a; Fu et al. 2012; Smith et al. 2010; Rosario et al. 2011). Using a complementary approach based on a sample of 1286 AGN pairs with projected separations < 100 kpc and velocity offsets < 600 km s⁻¹, Liu et al. (2011) have found a similar result of $\gtrsim 0.5\%$ for the frequency of binary AGNs on kpc scales, although the sample is biased against pairs with projected separations < 5 kpc. These observed frequencies based on optical surveys have been well reproduced by the phenomenological model presented by Yu et al. (2011). The model calculates the number density of binary AGNs based on the observed galaxy merger rate and BH–bulge scaling relations, under the assumption that significant nuclear activity is triggered only in gas-rich mergers with central massive BHs and only when the nuclei are roughly within the half-light radius of each other.

The relatively low frequency of kpc-scale binary AGNs suggests that optical identification combined with X-ray confirmation may be more efficient than blind X-ray searches. While blind hard X-ray surveys are needed to fully address the incompleteness of optical identification (e.g., Koss et al. 2012), a robust determination of the frequency of kpc binary AGNs using existing hard X-ray surveys is still hampered by small sample statistics and poor angular resolution. While searches in the radio using Expanded Very Large Array and/or Very Long Baseline Array can probe much smaller scales (e.g., Tingay & Wayth 2011; Lazio et al. 2012), the null result from the comprehensive study of Burke-Spolaor (2011), based on archival very long baseline interferometry observations of 3114 radio-luminous AGNs, may indicate that the detection yield could be strongly limited by the requirement of both AGNs being radio loud and the complication created by hot spots in radio jets.

6. SUMMARY

We have presented *HST*/WFC3 F336W and F105W imaging and *Chandra* ACIS-S 0.5–10 keV imaging spectroscopy of the four optically selected kpc-scale binary AGNs identified by Liu et al. (2010a). We have further clarified the ambiguities concerning the nature of the ionizing sources in optically selected kpc-scale binary AGNs. We summarize our main findings as follows.

1. By combining X-ray imaging spectroscopy and star formation constraints from high-resolution *U*-band imaging, we have critically examined the nature of the ionizing sources in the four optically selected kpc-scale binary AGNs. Our new *Chandra* and *HST* observations confirm the binary-AGN scenario for two of the four targets (SDSS J1108+0659 and SDSS J1146+5110). For the other two targets (SDSS J1131–0204 and SDSS J1332+0606), the existing data are still consistent with the binary-AGN scenario, although the possibility of only one AGN ionizing both components in the mergers cannot be ruled out. While the new observations lend some further support to identifying optical kpc-scale binary AGNs from a sample of optical candidates with double-peaked NELs, they also

¹⁶ Our parent AGN sample was selected from the SDSS DR7 main galaxy sample (Strauss et al. 2002), supplemented with Type 2 quasars from Reyes et al. (2008) that were not included in the main galaxy sample. The main galaxy sample includes objects with redshifts $z < 0.7$ and spectral classification as galaxies by the specBS pipeline (Adelman-McCarthy et al. 2008), or quasars that were targeted as galaxies. While Hao et al. (2005) have shown that the narrow emission line ratios of Type 1 AGNs also follow the Kewley et al. (2001) criteria, our parent AGN sample will miss (luminous) Type 1 AGNs that were not included in the DR7 main galaxies.

suggest that X-ray confirmation of optical binary candidates can be challenging and ambiguous, at least for heavily absorbed sources.

2. Combining our previous optical spectroscopy with the new X-ray observations, we have found tentative evidence for a systematically smaller hard-X-ray-to-[O III] luminosity ratio and/or higher Compton-thick fraction in optically selected kpc-scale binary AGNs than in optically selected single Type 2 Seyferts. We suggest that the observed X-ray weak distinction may be caused by a combination of higher nuclear gas column (possibly induced by mergers) and viewing angle bias (related to the double-peak NEL selection).

X-ray observations of more kpc-scale binary-AGN candidates are clearly needed to put our results on firmer statistical ground. Building a much larger sample would also enable the exploration of X-ray properties of kpc-scale binary AGNs as a function of separation and host galaxy properties. While deeper X-ray imaging of our targets would help better constrain their X-ray spectral properties, the required observations for robust spectral modeling (i.e., >200 counts) would be too expensive (likely at least 10 times our exposure times for targets at similar redshifts with comparable [O III] luminosities) to justify even for a small sample. Using a different approach, we are conducting a pilot imaging program with *Chandra* for a few kpc-scale binary AGNs at lower redshifts drawn from the parent sample of Liu et al. (2011). These observations will help better address to what extent the X-ray weak tendency in optically selected kpc-scale binary AGNs is caused by a viewing angle bias related to double-peak narrow-line selection (i.e., as opposed to a merger-driven gas concentration effect).

The obscured nature of the four optically selected kpc-scale binary AGNs allows us to study their host galaxy stellar populations without much contamination from the AGN itself. In Paper II, we will use *HST* WFC3 F105W and F336W imaging to characterize the detailed host galaxy morphologies and small-scale star formation properties. We will also address the properties and origins of the extended soft X-ray emission detected in SDSS J1108+0659, to better understand starburst, shock heating, outflows, and photoionization of gas on galactic-wide scales in kpc-scale binary AGNs.

We thank Markos Trichas for his generous help with providing the X-ray luminosity measurement of the CSC-SDSS cross-match AGN catalog reported in Trichas et al. (2012), and an anonymous referee for a careful and useful report that improved the paper.

Support for the work of X.L. was provided by NASA through Einstein Postdoctoral Fellowship grant number PF0-110076 awarded by the Chandra X-ray Center, which is operated by the Smithsonian Astrophysical Observatory for NASA under contract NAS8-03060. Y.S. acknowledges support through the Smithsonian Astrophysical Observatory from a Clay Postdoctoral Fellowship. M.A.S. acknowledges the support of NSF grant AST-0707266.

Support for this work was provided by NASA through Chandra Award Number GO1-12127X issued by the Chandra X-ray Observatory Center, which is operated by the Smithsonian Astrophysical Observatory for and on behalf of NASA under contract NAS 8-03060. Support for program number GO 12363 was provided by NASA through a grant from the Space Telescope Science Institute, which is operated by the Association of

Universities for Research in Astronomy, Inc., under NASA contract NAS 5-26555.

This research has made use of software provided by the Chandra X-ray Center in the application packages CIAO, ChIPS, and Sherpa.

Funding for the SDSS and SDSS-II has been provided by the Alfred P. Sloan Foundation, the Participating Institutions, the National Science Foundation, the U.S. Department of Energy, the National Aeronautics and Space Administration, the Japanese Monbukagakusho, the Max Planck Society, and the Higher Education Funding Council for England. The SDSS Web site is <http://www.sdss.org/>.

The SDSS is managed by the Astrophysical Research Consortium for the Participating Institutions. The Participating Institutions are the American Museum of Natural History, Astrophysical Institute Potsdam, University of Basel, University of Cambridge, Case Western Reserve University, University of Chicago, Drexel University, Fermilab, the Institute for Advanced Study, the Japan Participation Group, Johns Hopkins University, the Joint Institute for Nuclear Astrophysics, the Kavli Institute for Particle Astrophysics and Cosmology, the Korean Scientist Group, the Chinese Academy of Sciences (LAMOST), Los Alamos National Laboratory, the Max-Planck-Institute for Astronomy (MPIA), the Max-Planck-Institute for Astrophysics (MPA), New Mexico State University, Ohio State University, University of Pittsburgh, University of Portsmouth, Princeton University, the United States Naval Observatory, and the University of Washington.

Facilities: CXO (ACIS), HST (WFC3), Sloan

REFERENCES

- Abazajian, K., Adelman-McCarthy, J. K., Agüeros, M. A., et al. 2003, *AJ*, **126**, 2081
- Abazajian, K. N., Adelman-McCarthy, J. K., & Agüeros, M. A. 2009, *ApJS*, **182**, 543
- Abolmasov, P., Fabrika, S., Sholukhova, O., & Afanasiev, V. 2007, *AstBu*, **62**, 36
- Adelman-McCarthy, J. K., Agüeros, M. A., Allam, S. S., et al. 2008, *ApJS*, **175**, 297
- Antonucci, R. 1993, *ARA&A*, **31**, 473
- Axon, D. J., Marconi, A., Capetti, A., et al. 1998, *ApJL*, **496**, 75
- Baldwin, J. A., Phillips, M. M., & Terlevich, R. 1981, *PASP*, **93**, 5
- Ballet, J. 1999, *A&AS*, **135**, 371
- Ballo, L., Braitto, V., Della Ceca, R., et al. 2004, *ApJ*, **600**, 634
- Barrows, R. S., Stern, D., Madsen, K., et al. 2012, *ApJ*, **744**, 7
- Barth, A. J., Bentz, M. C., Greene, J. E., & Ho, L. C. 2008, *ApJL*, **683**, 119
- Bassani, L., Dadina, M., Maiolino, R., et al. 1999, *ApJS*, **121**, 473
- Begelman, M. C., Blandford, R. D., & Rees, M. J. 1980, *Natur*, **287**, 307
- Bell, E. F. 2003, *ApJ*, **586**, 794
- Bennert, N., Falcke, H., Schulz, H., Wilson, A. S., & Wills, B. J. 2002, *ApJL*, **574**, 105
- Bianchi, S., Chiaberge, M., Piconcelli, E., Guainazzi, M., & Matt, G. 2008, *MNRAS*, **386**, 105
- Blecha, L., Civano, F., Elvis, M., & Loeb, A. 2012a, arXiv:1205.6202
- Blecha, L., Loeb, A., & Narayan, R. 2012b, arXiv:1201.1904
- Brassington, N. J., Ponman, T. J., & Read, A. M. 2007, *MNRAS*, **377**, 1439
- Bruzual, G., & Charlot, S. 2003, *MNRAS*, **344**, 1000
- Burke-Spolaor, S. 2011, *MNRAS*, **410**, 2113
- Cardelli, J. A., Clayton, G. C., & Mathis, J. S. 1989, *ApJ*, **345**, 245
- Carter, C., Karovska, M., Jerius, D., Glotfelty, K., & Beikman, S. 2003, in ASP Conf. Ser. 295, *Astronomical Data Analysis Software and Systems XII*, ed. H. E. Payne, R. I. Jedrzejewski, & R. N. Hook (San Francisco, CA: ASP), 477
- Chabrier, G. 2003, *PASP*, **115**, 763
- Ciotti, L., & Ostriker, J. P. 2007, *ApJ*, **665**, 1038
- Ciotti, L., Ostriker, J. P., & Proga, D. 2010, *ApJ*, **717**, 708
- Civano, F., Elvis, M., Lanzuisi, G., et al. 2010, *ApJ*, **717**, 209
- Civano, F., Elvis, M., Lanzuisi, G., et al. 2012, *ApJ*, **752**, 49
- Collinge, M. J., Strauss, M. A., Hall, P. B., et al. 2005, *AJ*, **129**, 2542

- Colpi, M., & Dotti, M. 2011, *ASL*, **4**, 181
- Comerford, J. M., Gerke, B. F., Newman, J. A., et al. 2009a, *ApJ*, **698**, 956
- Comerford, J. M., Gerke, B. F., Stern, D., et al. 2012, *ApJ*, **753**, 42
- Comerford, J. M., Griffith, R. L., Gerke, B. F., et al. 2009b, *ApJL*, **702**, 82
- Comerford, J. M., Pooley, D., Gerke, B. F., & Madejski, G. M. 2011, *ApJL*, **737**, 19
- Cram, L., Hopkins, A., Mobasher, B., & Rowan-Robinson, M. 1998, *ApJ*, **507**, 155
- Crenshaw, D. M., Schmitt, H. R., Kraemer, S. B., Mushotzky, R. F., & Dunn, J. P. 2010, *ApJ*, **708**, 419
- Dickey, J. M., & Lockman, F. J. 1990, *ARA&A*, **28**, 215
- Djorgovski, S. 1991, in ASP Conf. Ser. 21, *The Space Distribution of Quasars*, ed. D. Crampton (San Francisco, CA: ASP), 349
- Dressel, L. (ed.) 2010, *Wide Field Camera 3 Instrument Handbook*, Version 3.0 (Baltimore, STScI)
- Ellison, S. L., Patton, D. R., Mendel, J. T., & Scudder, J. M. 2011, *MNRAS*, **418**, 2043
- Eracleous, M., Shields, J. C., Chartas, G., & Moran, E. C. 2002, *ApJ*, **565**, 108
- Evans, D. A., Lee, J. C., Kamenetska, M., et al. 2006, *ApJ*, **653**, 1121
- Evans, I. N., Primini, F. A., Glotfelty, K. J., et al. 2010, *ApJS*, **189**, 37
- Fabbiano, G. 2006, *ARA&A*, **44**, 323
- Fabbiano, G., Wang, J., Elvis, M., & Risaliti, G. 2011, *Natur*, **477**, 431
- Faber, S. M., Tremaine, S., Ajhar, E. A., et al. 1997, *AJ*, **114**, 1771
- Fischer, T. C., Crenshaw, D. M., Kraemer, S. B., et al. 2011, *ApJ*, **727**, 71
- Freeman, P., Doe, S., & Siemiginowska, A. 2001, *Proc. SPIE*, **4477**, 76
- Freeman, P. E., Kashyap, V., Rosner, R., & Lamb, D. Q. 2002, *ApJS*, **138**, 185
- Fruscione, A., McDowell, J. C., Allen, G. E., et al. 2006, *Proc. SPIE*, **6270**, 62701V
- Fu, H., Myers, A. D., Djorgovski, S. G., & Yan, L. 2011a, *ApJ*, **733**, 103
- Fu, H., Yan, L., Myers, A. D., et al. 2012, *ApJ*, **745**, 67
- Fu, H., Zhang, Z.-Y., Assef, R. J., et al. 2011b, *ApJL*, **740**, 44
- Garmire, G. P., Bautz, M. W., Ford, P. G., Nousek, J. A., & Ricker, G. R., Jr. 2003, *Proc. SPIE*, **4851**, 28
- Ge, J.-Q., Hu, C., Wang, J.-M., Bai, J.-M., & Zhang, S. 2012, *ApJS*, **201**, 31
- Gehrels, N. 1986, *ApJ*, **303**, 336
- Gerke, B. F., Newman, J. A., Lotz, J., et al. 2007, *ApJL*, **660**, 23
- Graham, A. W. 2004, *ApJL*, **613**, 33
- Green, P. J., Aldcroft, T. L., Richards, G. T., et al. 2009, *ApJ*, **690**, 644
- Green, P. J., Myers, A. D., Barkhouse, W. A., et al. 2010, *ApJ*, **710**, 1578
- Green, P. J., Myers, A. D., Barkhouse, W. A., et al. 2011, *ApJ*, **743**, 81
- Greene, J. E., Zakamska, N. L., Ho, L. C., & Barth, A. J. 2011, *ApJ*, **732**, 9
- Greene, J. E., Zakamska, N. L., & Smith, P. S. 2012, *ApJ*, **746**, 86
- Grimm, H.-J., Gilfanov, M., & Sunyaev, R. 2003, *MNRAS*, **339**, 793
- Guainazzi, M., Matt, G., Antonelli, L. A., et al. 1999, *MNRAS*, **310**, 10
- Guainazzi, M., Piconcelli, E., Jiménez-Bailón, E., & Matt, G. 2005, *A&A*, **429**, L9
- Hao, L., Strauss, M. A., Tremonti, C. A., et al. 2005, *AJ*, **129**, 1783
- Heckman, T. M., Miley, G. K., van Breugel, W. J. M., & Butcher, H. R. 1981, *ApJ*, **247**, 403
- Heckman, T. M., Ptak, A., Hornschemeier, A., & Kauffmann, G. 2005, *ApJ*, **634**, 161
- Hennawi, J. F., Myers, A. D., Shen, Y., et al. 2010, *ApJ*, **719**, 1672
- Hennawi, J. F., Strauss, M. A., Oguri, M., et al. 2006, *AJ*, **131**, 1
- Hernquist, L. 1989, *Natur*, **340**, 687
- Ho, L. C., Filippenko, A. V., & Sargent, W. L. 1995, *ApJS*, **98**, 477
- Høg, E., Fabricius, C., Makarov, V. V., et al. 2000, *A&A*, **355**, L27
- Hopkins, A. M., Miller, C. J., Nichol, R. C., et al. 2003, *ApJ*, **599**, 971
- Hopkins, P. F., Hernquist, L., Cox, T. J., & Kereš, D. 2008, *ApJS*, **175**, 356
- Hudson, D. S., Reiprich, T. H., Clarke, T. E., & Sarazin, C. L. 2006, *A&A*, **453**, 433
- Jansen, F., Lumb, D., Altieri, B., et al. 2001, *A&A*, **365**, L1
- Jiménez-Bailón, E., Loiseau, N., Guainazzi, M., et al. 2007, *A&A*, **469**, 881
- Junkkarinen, V., Shields, G. A., Beaver, E. A., et al. 2001, *ApJL*, **549**, 155
- Kennicutt, R. C., Jr. 1998, *ARA&A*, **36**, 189
- Kewley, L. J., Dopita, M. A., Sutherland, R. S., Heisler, C. A., & Trevena, J. 2001, *ApJ*, **556**, 121
- Kochanek, C. S., Falco, E. E., & Muñoz, J. A. 1999, *ApJ*, **510**, 590
- Komossa, S., Burwitz, V., Hasinger, G., et al. 2003, *ApJL*, **582**, 15
- Kormendy, J., & Bender, R. 2009, *ApJL*, **691**, 142
- Kormendy, J., & Richstone, D. 1995, *ARA&A*, **33**, 581
- Koss, M., Mushotzky, R., Treister, E., et al. 2011, *ApJL*, **735**, 42
- Koss, M., Mushotzky, R., Treister, E., et al. 2012, *ApJL*, **746**, 22
- Kroupa, P. 2001, *MNRAS*, **322**, 231
- Lazio, T. J. W., Liu, X., Shen, Y., & Strauss, M. A. 2012, *ApJ*, in press
- Levenson, N. A., Krolak, J. H., Życki, P. T., et al. 2002, *ApJL*, **573**, 81
- Li, J., Kastner, J. H., Prigozhin, G. Y., et al. 2004, *ApJ*, **610**, 1204
- Liu, X., Greene, J. E., Shen, Y., & Strauss, M. A. 2010a, *ApJL*, **715**, 30
- Liu, X., Shen, Y., Peng, C. Y., et al. 2012a, *ApJ*, in press
- Liu, X., Shen, Y., & Strauss, M. A. 2012b, *ApJ*, **745**, 94
- Liu, X., Shen, Y., Strauss, M. A., & Greene, J. E. 2010b, *ApJ*, **708**, 427
- Liu, X., Shen, Y., Strauss, M. A., & Hao, L. 2011, *ApJ*, **737**, 101
- Liu, X., Zakamska, N. L., Greene, J. E., et al. 2009, *ApJ*, **702**, 1098
- Long, K. S., & van Speybroeck, L. P. 1983, in *Accretion-Driven Stellar X-ray Sources*, ed. W. H. G. Lewin & E. P. J. van den Heuvel (Cambridge: Cambridge Univ. Press), 117
- Lutz, D., Veilleux, S., & Genzel, R. 1999, *ApJL*, **517**, 13
- Ma, C., Arias, E. F., Eubanks, T. M., et al. 1998, *AJ*, **116**, 516
- Matt, G., Guainazzi, M., Frontera, F., et al. 1997, *A&A*, **325**, L13
- Mazzarella, J. M., & Boroson, T. A. 1993, *ApJS*, **85**, 27
- Mazzarella, J. M., Iwasawa, K., Vavilkin, T., et al. 2012, *AJ*, **144**, 125
- McGurk, R. C., Max, C. E., Rosario, D. J., et al. 2011, *ApJL*, **738**, 2
- Merritt, D. 2006, *RPPH*, **69**, 2513
- Miller, J. M., Fabbiano, G., Miller, M. C., & Fabian, A. C. 2003, *ApJL*, **585**, 37
- Miller, M. C., & Colbert, E. J. M. 2004, *IJMPD*, **13**, 1
- Milosavljević, M., & Merritt, D. 2001, *ApJ*, **563**, 34
- Moran, E. C., Halpern, J. P., Bothun, G. D., & Becker, R. H. 1992, *AJ*, **104**, 990
- Mortlock, D. J., Webster, R. L., & Francis, P. J. 1999, *MNRAS*, **309**, 836
- Mulchaey, J. S., Koratkar, A., Ward, M. J., et al. 1994, *ApJ*, **436**, 586
- Myers, A. D., Brunner, R. J., Richards, G. T., et al. 2007, *ApJ*, **658**, 99
- Nandra, K., & Pounds, K. A. 1994, *MNRAS*, **268**, 405
- Oke, J. B. 1974, *ApJS*, **27**, 21
- Osterbrock, D. E. 1989, *Astrophysics of Gaseous Nebulae and Active Galactic Nuclei* (Research Supported by the University of California, John Simon Guggenheim Memorial Foundation, University of Minnesota, et al.; Mill Valley, CA: Univ. Science Books), 422
- Panessa, F., Bassani, L., Cappi, M., et al. 2006, *A&A*, **455**, 173
- Park, T., Kashyap, V. L., Siemiginowska, A., et al. 2006, *ApJ*, **652**, 610
- Peng, Z.-X., Chen, Y.-M., Gu, Q.-S., & Hu, C. 2011, *RAA*, **11**, 411
- Piconcelli, E., Vignali, C., Bianchi, S., et al. 2010, *ApJL*, **722**, 147
- Ptak, A., Heckman, T., Levenson, N. A., Weaver, K., & Strickland, D. 2003, *ApJ*, **592**, 782
- Ptak, A., Zakamska, N. L., Strauss, M. A., et al. 2006, *ApJ*, **637**, 147
- Ranalli, P., Comastri, A., & Setti, G. 2003, *A&A*, **399**, 39
- Ravindranath, S., Ho, L. C., & Filippenko, A. V. 2002, *ApJ*, **566**, 801
- Revnivtsev, M., Sazonov, S., Jahoda, K., & Gilfanov, M. 2004, *A&A*, **418**, 927
- Reyes, R., Zakamska, N. L., Strauss, M. A., et al. 2008, *AJ*, **136**, 2373
- Richardson, J., Zheng, Z., Chatterjee, S., Nagai, D., & Shen, Y. 2012, *ApJ*, **755**, 30
- Risaliti, G., Maiolino, R., & Salvati, M. 1999, *ApJ*, **522**, 157
- Rosario, D. J., McGurk, R. C., Max, C. E., et al. 2011, *ApJ*, **739**, 44
- Rosario, D. J., Shields, G. A., Taylor, G. B., Salvander, S., & Smith, K. L. 2010, *ApJ*, **716**, 131
- Salpeter, E. E. 1955, *ApJ*, **121**, 161
- Sargent, W. L. W. 1972, *ApJ*, **173**, 7
- Sazonov, S. Y., & Revnivtsev, M. G. 2004, *A&A*, **423**, 469
- Scalo, J. M. 1986, *FCPh*, **11**, 1
- Schmitt, H. R., Donley, J. L., Antonucci, R. R. J., et al. 2003, *ApJ*, **597**, 768
- Shen, Y., Hennawi, J. F., Shankar, F., et al. 2010, *ApJ*, **719**, 1693
- Shen, Y., Liu, X., Greene, J. E., & Strauss, M. A. 2011a, *ApJ*, **735**, 48
- Shen, Y., Richards, G. T., Strauss, M. A., et al. 2011b, *ApJS*, **194**, 45
- Shields, G. A., Rosario, D. J., Junkkarinen, V., et al. 2012, *ApJ*, **744**, 151
- Silverman, J. D., Kampczyk, P., Jahnke, K., et al. 2011, *ApJ*, **743**, 2
- Smith, K. L., Shields, G. A., Bonning, E. W., et al. 2010, *ApJ*, **716**, 866
- Smith, K. L., Shields, G. A., Salvander, S., Stevens, A. C., & Rosario, D. J. 2011, arXiv:1108.0383
- Smith, K. L., Shields, G. A., Salvander, S., Stevens, A. C., & Rosario, D. J. 2012, *ApJ*, **752**, 63
- Strauss, M. A., Weinberg, D. H., Lupton, R. H., et al. 2002, *AJ*, **124**, 1810
- Strickland, D. K., & Stevens, I. R. 2000, *MNRAS*, **314**, 511
- Tadhunter, C., Ramos Almeida, C., Morganti, R., et al. 2012, *MNRAS*, **427**, 1603
- Teng, S. H., Schawinski, K., Urry, C. M., et al. 2012, *ApJ*, **753**, 165
- Teng, S. H., Wilson, A. S., Veilleux, S., et al. 2005, *ApJ*, **633**, 664
- Terashima, Y., Ho, L. C., & Ptak, A. F. 2000, *ApJ*, **539**, 161
- Thorne, K. S. 1987, in *Gravitational Radiation, 300 Years of Gravitation*, ed. S. W. Hawking & W. Israel (Cambridge: Cambridge Univ. Press), 330
- Thorne, K. S., & Braginskii, V. B. 1976, *ApJL*, **204**, 1
- Tingay, S. J., & Wayth, R. B. 2011, *AJ*, **141**, 174
- Trichas, M., Green, P. J., Silverman, J. D., et al. 2012, *ApJS*, **200**, 17
- Turner, T. J., George, I. M., Nandra, K., & Mushotzky, R. F. 1997a, *ApJS*, **113**, 23
- Turner, T. J., George, I. M., Nandra, K., & Mushotzky, R. F. 1997b, *ApJ*, **488**, 164
- Urry, C. M., & Padovani, P. 1995, *PASP*, **107**, 803

- Van Wassenhove, S., Volonteri, M., Mayer, L., et al. 2012, *ApJL*, 748, 7
- Veilleux, S., Shopbell, P. L., & Miller, S. T. 2001, *AJ*, 121, 198
- Vignati, P., Molendi, S., Matt, G., et al. 1999, *A&A*, 349, L57
- Wang, J., Chen, Y., Hu, C., et al. 2009, *ApJL*, 705, 76
- Weisskopf, M. C., O'dell, S. L., & van Speybroeck, L. P. 1996, *Proc. SPIE*, 2805, 2
- Whittle, M. 1992, *ApJS*, 79, 49
- Whittle, M., & Wilson, A. S. 2004, *AJ*, 127, 606
- Wolfe, A. M. (ed.) 1978, Pittsburgh Conference on BL Lac Objects, April 24–26 1978 (Pittsburgh, PA: Univ. Pittsburgh)
- Xu, C., Livio, M., & Baum, S. 1999, *AJ*, 118, 1169
- Xu, D., & Komossa, S. 2009, *ApJL*, 705, 20
- York, D. G., Adelman, J., Anderson, J. E., Jr., et al. 2000, *AJ*, 120, 1579
- Young, A. J., Wilson, A. S., & Shopbell, P. L. 2001, *ApJ*, 556, 6
- Yu, Q. 2002, *MNRAS*, 331, 935
- Yu, Q., Lu, Y., Mohayaee, R., & Colin, J. 2011, *ApJ*, 738, 92
- Zakamska, N. L., Strauss, M. A., Krolik, J. H., et al. 2003, *AJ*, 126, 2125
- Zakamska, N. L., Strauss, M. A., Krolik, J. H., et al. 2006, *AJ*, 132, 1496
- Zezas, A., Alonso-Herrero, A., & Ward, M. J. 2001, *Ap&SS*, 276, 601
- Zhou, H., Wang, T., Zhang, X., Dong, X., & Li, C. 2004, *ApJL*, 604, 33